The dynamics of supersonic flow past a new cusped leading edge airfoil

Saif Akram, Nadeem Hasan

The dynamics of supersonic flow past a new cusped leading edge airfoil

Saif Akram*

Department of Mechanical Engineering,
National Institute of Technology Durgapur,
M.G. Avenue, Durgapur-713209, West Bengal, India
Email: saif.akram@me.nit.ac.in
Email: saifakram.akram@gmail.com
*Corresponding author

Nadeem Hasan

Department of Mechanical Engineering,
Aligarh Muslim University,
Aligarh-202001, Uttar Pradesh, India
Email: n.hasan.me@amu.ac.in

Abstract: A new family of cusped leading edge airfoil with great implications in supersonic aircraft design has been proposed in this work. Numerical investigation of unsteady, viscous and laminar compressible flow past the new cusped leading edge airfoil and a conventional biconvex airfoil with the same maximum thickness is carried out and a systematic comparison of the aerodynamic parameters are reported. The value of Reynolds number is held constant which is 5×10^5 and the Mach number is varied from 1.25 to 2.13. The results are computed at three different angles of attack given as $\alpha = 0°$, $\alpha = 10°$ and $\alpha = 20°$. The comparison of aerodynamic parameters of the new airfoil with that of conventional biconvex supersonic airfoil shows that the new airfoil is much superior to the conventional airfoil. The L/D ratio of the new airfoil is higher than the biconvex circular-arc airfoil for almost all the flight conditions.

Keywords: cusped leading edge airfoil; CFD; drag reduction; supersonic flow.

Biographical notes: Saif Akram is an Assistant Professor in the Department of Mechanical Engineering, National Institute of Technology Durgapur, West Bengal, India. He obtained his PhD in High Speed Aerodynamics Laboratory from the Indian Institute of Technology Kanpur, India in 2018. His research interests include experimental aerodynamics and aeroacoustics, CFD, supersonic jets, shock mitigation and noise control.

Nadeem Hasan is a Professor in the Department of Mechanical Engineering, ZHCET, Aligarh Muslim University, India. He obtained his PhD in Computational Fluid Mechanics and Heat Transfer from the Indian Institute of Technology Delhi, India in 2006. His research interests include computer simulation of problems involving incompressible fluid flow and heat transfer and analysis of bifurcations and instabilities.

1 Introduction

The strong normal shock waves customarily present near the blunt leading edges of airfoils leads to high wave drag (Bushnell, 2004). For these situations, the normal and simple wave drag reduction solution is simply to reduce the diameter of the leading edge with a sharp nose. But, the heating associated with higher speeds generally limits the degree of sharpness that is technically attainable, as do different stringent operational safety and power. Therefore, scientists look for an alternative to physical bluntness such as a nose-positioned flow-through channel that can be treated as an unstarted inlet, resulting in a standoff shock system (Gupta and Ruffin, 1999; Gupta et al., 2000; Ruffin et al., 2000). Another methodology of reducing the high wave drag owing to blunt leading edges is to artificially sharpen the region. To achieve this, many design modifications have been proposed which includes

physical nose spikes (Garanin, 2000; Gilinsky et al., 2001; Guy et al., 2001; Jones et al., 2000; Karlovskii and Sakharov, 1986; Kijima et al., 1996; Reding et al., 1977; Reding and Jecmen, 1983; Yamauchi et al., 1993), upstream gas injection (Charczenko and Hennessey, 1961; Love, 1952; Meyer et al., 2001; Romeo and Sterrett, 1963), liquid (Bushnell and Huffman, 1968), and perhaps even solids/particulates, and upstream focused heating/energy projection/addition (Geoggievskii and Lenin, 1988; Golovitchev and Hansson, 1998; Myrabo and Raizer, 1994; Riggins et al., 1999; Riggins and Nelson, 2000).

Some of the recent prominent works on aerodynamic parameters of high speed airfoils include lift sensitivity analysis for a Whitcomb airfoil with aileron deflections (Kuzmin, 2015), computational study of supersonic flow past non-stationary obstructions (Deshpande et al., 2015), optimisation of swept angles for airfoil NACA 6-series (Selvaraj et al., 2017), effect of the angle of attack on the YF-16 inlet (Ibrahim et al., 2010), critical assessment of hybrid and zonal wall functions for missile aerodynamics simulations (Walters and Blades, 2011), etc.

Several contour modifications have been adopted in addition to the drag reduction approaches mentioned above. One of the most commonly used methods is the supercritical wing for transonic flow (Whitcomb, 1974; Raj and Miranda, 1981; Ayers and Hallissy, 1981). Another contour modification is the use of local passive porosity unlike the usual impervious surface boundary condition (Bahi et al., 1983; Bur et al., 1998; Chen et al., 1985; Gillan, 1993; Hsieh and Lee, 1989; Raghunathan, 1987; Raghunathan et al., 1987). A third way of reducing the wave drag is the use of localised morphing bumps or local wall deformations (Ashill et al., 1996; Reneaux and Coustols, 1999; Rosemann et al., 2000; Schmitt and Destarac, 1998) and adaptive airfoils or smart wings (Redeker et al., 1986). Several other contour modifications like reduction of profile drag at supersonic velocities by the use of airfoil sections having a blunt trailing edge (Chapman, 1955), castellated blunt trailing edge (Magi and Gai, 1998), asymmetric biconvex circular-arc airfoil (Akram et al., 2013), flattened airfoils (Alexander, 2008), etc. have been studied. A detailed review on the shock wave drag reduction approaches is available in Bushnell (2004).

The contribution to the high aerodynamic drag in supersonic flow comes primarily from the formation of shock waves at the leading edge. For an airfoil having a finite leading edge angle, the formation of attached/detached shocks is controlled by the flight Mach number in the supersonic regime. In fact, for a given leading edge angle 'δ', there is a minimum Mach number in the supersonic regime for the formation of attached oblique shocks at the leading edge. Attached shocks lead to lower pressure downstream of the shock than for the case of detached shocks. Therefore, leading edge flow modification can also provide significant alteration to the drag characteristics of an airfoil in the supersonic flow regime. In the present work, the aerodynamic performance

of a new cusped leading edge airfoil ($\delta = 0°$) specifically designed with the aim of reducing the wave drag in supersonic flow regime is investigated. As shown in Figure 1, the formation of cusped leading edge necessitates the use of a combination of a concave and a convex shaped curves to represent the entire upper and lower surface of the airfoil. The convex portion and the concave portion meet at the point of maximum thickness located at (x_m, 0) along the chord. The geometry is specified by three control parameters, h, a and x_m as fractions of the chord length c. The geometry of the concave portion OA is chosen to be represented by a cubic polynomial:

$$y_{OA}(x) = a_1 x^2 + a_2 x^3, \qquad 0 \leq x \leq x_m \qquad (1)$$

The convex portion AC is chosen to be represented by a circular arc governed by the equation:

$$y_{AC}(x) = \left(\frac{h}{2} - \frac{a^2}{2h} \right)$$
$$+ \sqrt{\left(\frac{a^2}{2h} + \frac{h}{2} \right)^2 - (x - 1 + a)^2}, \qquad (2)$$
$$x_m \leq x \leq 1$$

Figure 1   Geometry of the new symmetric cusped leading edge airfoil
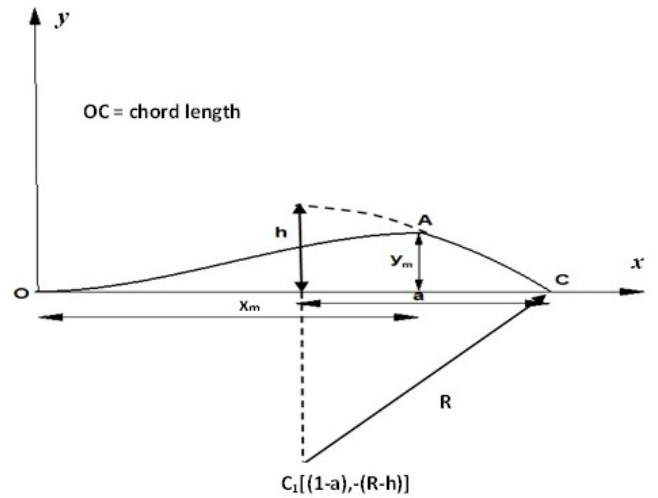
Where h is the maximum thickness of the circular arc located at a distance a from the trailing edge along the chord. The constants 'a_1' and 'a_2' in equation (1) are determined from the constraints at $x = x_m$ given as:

$$y_{OA}(x_m) = y_{AC}(x_m) = \alpha_1$$
$$\frac{dy_{OA}}{dx} = 0 \quad \text{at} \quad x = x_m \qquad (3)$$

The values of 'a_1' and 'a_2' are found to be:

$$a_1 = \frac{3\alpha_1}{x_m^2}$$
$$a_2 = -\frac{2\alpha_1}{x_m^3} \qquad (4)$$

Here, 'y_m' is the maximum thickness of the airfoil located at a distance of 'x_m' from the leading edge. Although this method of controlling the maximum thickness of the airfoil leads to a slight discontinuity at the point of joining of the two curves, but this route is opted as it gives a better control on the location of maximum thickness and the point of joining of the concave and convex curves can be easily varied leading to a new family of cusped leading edge airfoils. Moreover, the current design of airfoil might generate high heat flux at the nose. This is a matter of further investigation (Banas, 2020) and right now our main focus is the potential aerodynamic benefits.

2 Mathematical formulation and numerical method

2.1 Governing equations

To investigate the compressible flow past an airfoil, the two-dimensional compressible Navier-Stokes equations in generalised coordinates are employed. The two-dimensional, unsteady, compressible Navier-Stokes equations are a set of four coupled, nonlinear partial differential equations. The most general equations governing the unsteady, compressible gas dynamics in dimensional framework can be expressed in strong conservative form as,

$$\frac{\partial \bar{U}}{\partial \bar{t}} + \frac{\partial \bar{F}}{\partial \bar{x}} + \frac{\partial \bar{G}}{\partial \bar{y}} = \bar{J} \tag{5}$$

where

$$\bar{U} = \begin{Bmatrix} \bar{\rho} \\ \bar{\rho}\bar{u} \\ \bar{\rho}\bar{v} \\ \bar{\rho}\bar{E} \end{Bmatrix},$$

$$\bar{F} = \begin{Bmatrix} \bar{\rho}\bar{u} \\ \bar{\rho}\bar{u}^2 + \bar{p} + \frac{2}{3}\bar{\mu}(\Delta.\vec{V}) - 2\bar{\mu}\frac{\partial \bar{u}}{\partial \bar{x}} \\ \bar{\rho}\bar{u}\bar{v} - \bar{\mu}\left(\frac{\partial \bar{v}}{\partial \bar{x}} + \frac{\partial \bar{u}}{\partial \bar{y}}\right) \\ \bar{\rho}\bar{u}\bar{h}_T - \bar{k}\frac{\partial \bar{T}}{\partial \bar{x}} + \Phi_F \end{Bmatrix},$$

$$\bar{G} = \begin{Bmatrix} \bar{\rho}\bar{v} \\ \bar{\rho}\bar{u}\bar{v} - \bar{\mu}\left(\frac{\partial \bar{v}}{\partial \bar{x}} + \frac{\partial \bar{u}}{\partial \bar{y}}\right) \\ \bar{\rho}\bar{v}^2 + \bar{p} + \frac{2}{3}\bar{\mu}(\Delta.\vec{V}) - 2\bar{\mu}\frac{\partial \bar{u}}{\partial \bar{x}} \\ \bar{\rho}\bar{v}\bar{h}_T - \bar{k}\frac{\partial \bar{T}}{\partial \bar{y}} + \Phi_G \end{Bmatrix},$$

$$\bar{J} = \begin{Bmatrix} 0 \\ 0 \\ 0 \\ 0 \end{Bmatrix} \tag{6}$$

In equations (5) and (6), the symbols $\bar{x}$, $\bar{y}$ represents Cartesian spatial coordinates and $\bar{t}$ is the time. The gravity term in $\bar{J}$ are dropped as they are generally very weak in high speed flows. The various primitive variables like density, temperature, thermodynamic pressure, velocity components, total specific energy are represented as $\bar{\rho}$, $\bar{T}$, $\bar{p}$, $(\bar{u}, \bar{v})$ and $\bar{E}$ respectively. The molecular transport properties like viscosity and thermal conductivity are represented as $\bar{\mu}$ and $\bar{k}$ respectively. $\bar{U}$ is the vector of conservative variables, and $\bar{F}$, $\bar{G}$ are total flux vectors. The quantities $\bar{\Phi}_F$ and $\bar{\Phi}_G$ appearing in the flux vectors $\bar{F}$ and $\bar{G}$ respectively are,

$$\Phi_F = \mu \left[\frac{2}{3}\bar{u}\left(\frac{\partial \bar{v}}{\partial \bar{y}} - \frac{2\partial \bar{u}}{\partial \bar{x}}\right) - \bar{v}\left(\frac{\partial \bar{v}}{\partial \bar{x}} + \frac{\partial \bar{u}}{\partial \bar{y}}\right)\right] \tag{7}$$

$$\Phi_G = \mu \left[\frac{2}{3}\bar{v}\left(\frac{\partial \bar{u}}{\partial \bar{x}} - \frac{2\partial \bar{v}}{\partial \bar{y}}\right) - \bar{u}\left(\frac{\partial \bar{v}}{\partial \bar{x}} + \frac{\partial \bar{u}}{\partial \bar{y}}\right)\right] \tag{8}$$

The total specific energy and enthalpy are defined as,

$$\bar{E} = \bar{e} + \frac{\bar{V}^2}{2}, \qquad \bar{h}_T = \bar{E} + \frac{\bar{p}}{\bar{\rho}} \tag{9}$$

The above system of equations is closed by bringing in the ideal (thermally and calorically perfect) gas assumption,

$$\bar{p} = \bar{\rho}R\bar{T}, \qquad \bar{e} = C_v\bar{T} \tag{10}$$

where C_v is the specific heat at constant volume and is given by,

$$C_v = R/(\gamma - 1)$$

where R is the universal gas constant and γ is the ratio of specific heats usually taken as 1.4.

The molecular viscosity is assumed to obey Sutherland's law given as,

$$\bar{\mu} = \mu_o \left(\frac{\bar{T}}{\bar{T}_o}\right)^{\frac{3}{2}} \left[\frac{\bar{T}_o + S}{\bar{T} + S}\right] \tag{11}$$

In the above equation S is the Sutherland constant, having a value of 110.56 K. μ_o is the reference viscosity and T_o is the reference temperature, having their respective values as 1.716×10^{-5} Kg/ms and 273.11 K. The value of thermal conductivity is fixed to 0.0242 w/mk which gives Prandtl number as 0.743.

To non-dimensionalise the equations, the free-stream variables including the density ρ_∞, temperature T_∞, pressure p_∞, velocity U_∞, viscosity μ_∞ and chord of the airfoil 'l' as characteristic scales are used. The non-dimensional parameters are defined as follows:

$$u = \frac{\bar{u}}{U_\infty}, \qquad v = \frac{\bar{v}}{U_\infty}, \qquad p = \frac{\bar{p}}{p_\infty}, \qquad T = \frac{\bar{T}}{T_\infty},$$

$$\rho = \frac{\bar{\rho}}{\rho_\infty}, \qquad \mu = \frac{\bar{\mu}}{\mu_\infty}, \qquad k = \frac{\bar{k}}{k_\infty}, \qquad x = \frac{\bar{x}}{L},$$

$$y = \frac{\bar{y}}{L}, \qquad t = \frac{\bar{t}L}{U_\infty}, \qquad e = \frac{\bar{e}}{C_{V_\infty}T_\infty},$$

$$E = \frac{\bar{E}}{C_{V_\infty}T_\infty} = e + \frac{\gamma(\gamma - 1)}{2}M^2(u^2 + v^2),$$

$$h_T = E + (\gamma - 1)\frac{p}{\rho}, \qquad C_p = \frac{p - p_\infty}{\frac{1}{2}\rho_\infty u_\infty^2},$$

$$C_D = \frac{D}{\frac{1}{2}\rho_\infty u_\infty^2 A}, \qquad C_L = \frac{L}{\frac{1}{2}\rho_\infty u_\infty^2 A},$$

$$C_m = \frac{M_o}{\frac{1}{2}\rho_\infty u_\infty^2 Al}$$

where A is the reference area $(1\,\mathrm{m}^2)$, l is the reference length (chord length), D is the drag force, L is the lift force and M_o is the pitching moment about leading edge of the airfoil.

With the scaling given above, the governing equations are modified as:

$$\frac{\partial U}{\partial t} + \frac{\partial F}{\partial x} + \frac{\partial G}{\partial y} = J \tag{12}$$

where

$$U = \begin{Bmatrix} \rho \\ \rho u \\ \rho v \\ \rho E \end{Bmatrix},$$

$$F = \begin{Bmatrix} \rho u \\ \rho u^2 + \frac{1}{\gamma M^2}p - \frac{2\mu}{Re}\left\{\frac{\partial u}{\partial x} - \frac{1}{3}(\Delta.\vec{V})\right\} \\ \rho uv - \frac{\mu}{Re}\left(\frac{\partial v}{\partial x} + \frac{\partial u}{\partial y}\right) \\ \rho u h_T - \frac{k}{RePr}\frac{\partial T}{\partial x} + \frac{\gamma(\gamma-1)M^2\mu}{Re}D_F \end{Bmatrix},$$

$$G = \begin{Bmatrix} \rho v \\ \rho uv - \frac{\mu}{Re}\left(\frac{\partial v}{\partial x} + \frac{\partial u}{\partial y}\right) \\ \rho v^2 + \frac{1}{\gamma M^2}p - \frac{2\mu}{Re}\left\{\frac{\partial v}{\partial y} - \frac{(\Delta.\vec{V})}{3}\right\} \\ \rho v h_T - \frac{k}{RePr}\frac{\partial T}{\partial y} + \frac{\gamma(\gamma-1)M^2\mu}{Re}D_G \end{Bmatrix}, \tag{13}$$

$$J = \begin{Bmatrix} 0 \\ 0 \\ 0 \\ 0 \end{Bmatrix}$$

where

$$D_F = \left[\frac{2}{3}u\left(\frac{\partial v}{\partial y} - 2\frac{\partial u}{\partial x}\right) - v\left(\frac{\partial v}{\partial x} + \frac{\partial u}{\partial y}\right)\right] \tag{14}$$

$$D_G = \left[\frac{2}{3}v\left(\frac{\partial u}{\partial x} - 2\frac{\partial v}{\partial y}\right) - u\left(\frac{\partial v}{\partial x} + \frac{\partial u}{\partial y}\right)\right] \tag{15}$$

The non-dimensional numbers used in the above equations are expressed as:

$$Re = \frac{\rho U_\infty l}{\mu}, \qquad Pr = \frac{\mu C_p}{k}$$

2.2 Numerical scheme

The governing equations are solved by using ANSYS Fluent which uses a control-volume-based technique (finite-volume method). The density-based solver was selected which solves the governing equations of continuity, momentum, and energy for a compressible flow simultaneously (i.e., coupled together). In the density-based solution methods, the discrete, nonlinear governing equations are linearised to produce a system of equations for the dependent variables in every computational cell. The resultant linear system is then solved to yield an updated flow-field solution. The governing equations are marched in time employing a second-order implicit discretisation scheme. The inviscid flux vector is evaluated by a standard upwind, Roe-flux difference splitting scheme. This approach acknowledges that the flux vector contains characteristic information propagating through the domain with speed and direction according to the eigenvalues of the system. By splitting into parts, where each part contains information travelling in a particular direction (i.e., characteristic information), and upwind interpolation of the split fluxes in a manner consistent with their corresponding eigenvalues, we obtain the expression for the discrete flux at each face. ANSYS Fluent stores discrete values of the scalar at the cell centres. However, face values are required for the convection terms and must be interpolated from the cell centre values. This is accomplished using a second order upwind scheme. Upwinding means that the face value is derived from quantities in the cell upstream, or 'upwind', relative to the direction of the normal velocity. When second-order accuracy is desired, quantities at cell faces are computed using a multidimensional linear reconstruction approach. In this approach, higher-order accuracy is achieved at cell faces through a Taylor series expansion of the cell-centred solution about the cell centroid. Thus when second-order upwinding is selected, the face value is computed using the following expression:

$$\phi_{f,SOU} = \phi + \nabla\phi.\vec{r} \tag{16}$$

where ϕ and $\nabla\phi$ are the cell-centred value and its gradient in the upstream cell, and is the displacement vector from the upstream cell centroid to the face centroid. This formulation requires the determination of the gradient in each cell. The gradients are computed according to the least squares cell-based method. The differentiable gradient limiter is used on the second-order upwind (SOU) scheme to prevent spurious oscillations, which would otherwise appear in the solution flow field near shocks, discontinuities, or near rapid local changes in the flow field. The gradient limiter attempts to invoke and enforce the monotonicity principle by prohibiting the linearly reconstructed field variable on the cell faces to exceed the maximum or minimum values of the neighbouring cells. ANSYS Fluent uses the scalar form of the gradient limiter given by the following equation:

$$\Phi_{f,SOU} = \Phi + \psi\nabla\phi.r \tag{17}$$

where ψ is a scalar value which limits the gradient $\nabla\phi$ (ANSYS, 2013) .

2.3 Boundary conditions

At the surface of the airfoil, the flow is governed by no-slip and no penetration condition for the velocity. Additional constraints on the fluid properties on the wall are brought in by specifying that the wall is adiabatic. Pressure far-field boundary condition is applied at both the inflow and the outflow. Pressure far-field conditions are used to model a free-stream condition at infinity, with free-stream Mach number and static conditions being specified. Angle of attack is specified by providing the components of flow direction. The pressure far-field boundary condition is often called a characteristic boundary condition, since

it uses characteristic information (Riemann invariants) to determine the flow variables at the boundaries.

The dimensional parameters which are provided as input to the solver depend upon the inflow conditions. For example, at a Mach number of 1.25 and angle of attack of 20°, the inputs are calculated as: $M = 1.25$, $Re = 5 \times 10^5$, $\alpha = 20°$, chord length of the airfoil is calculated from the airfoil geometry and is constant, c = 1 m, gauge pressure, P = 1,775.544 Pascal, temperature, T = 300 K, x-velocity = 407.6935 m/s, y-velocity = 148.3887 m/s, $\Delta t = 1 \times 10^{-5}$ s, specific heat (C_P) = 1,006.43 J/kg-k, thermal conductivity (K) = 0.0242 W/m-k, molecular weight = 28.966 kg/kmol, density is calculated from ideal gas equation, viscosity is calculated from Sutherland law.

3 Computational overview and validation

3.1 Geometry of the airfoil

In the present study, the aerodynamic characteristics of a new cusped leading edge airfoil are investigated. For this purpose, the geometry of the airfoil is recovered from equation (1)–(4). The geometric parameters are fixed as,

$$x_m = 0.75, \quad a = 0.5, \quad h = 0.065$$

For these parameters, the profile of the airfoil is shown in Figure 2. The airfoil has a maximum thickness $y_m = 0.05$ at a location $x_m = 0.75$ from the leading edge. The main control parameters for the present investigation are free stream Mach number (M) and angle of attack α. The Mach number is varied from 1.15 to 2.13 at three different angle of attacks of $\alpha = 0°, 10°$ and $20°$. The value of free stream Reynolds number is fixed to 5×10^5. Although, this is somewhat lower than the typical values of Re encountered during flight conditions that are in the range of 10^7 to 10^8, this value is chosen because it is computationally very demanding to resolve the relevant scales of a turbulent boundary layer at such a high Re. Besides, since a new family of cusped leading edge airfoils is under the scanner, it is worthwhile to investigate the performance at a lower Re possibly in the laminar regime in order to identify any potential aerodynamic benefits or performance improvements. Since the aerodynamic characteristics of the new airfoil geometry are to be compared with a conventional symmetric biconvex circular-arc airfoil, the geometry of a biconvex circular-arc airfoil is also generated. In order to generate the coordinates of the circular-arc airfoil, the equations governing the profile can be developed in a straight-forward manner. Figure 3 shows a typical geometry of the upper surface of a biconvex circular-arc airfoil.

Figure 2 Geometry of the new symmetric cusped leading edge airfoil
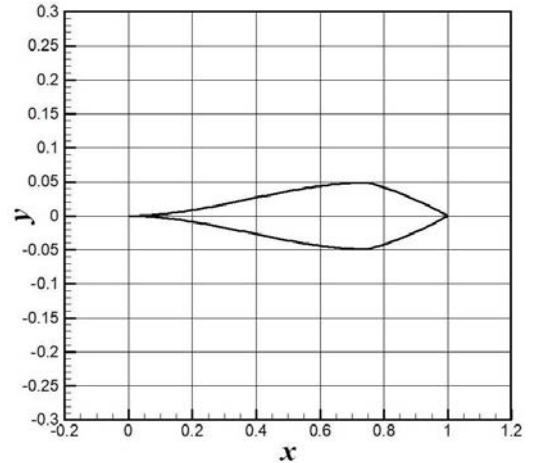
Figure 3 Geometry of the upper surface of a biconvex circular-arc airfoil
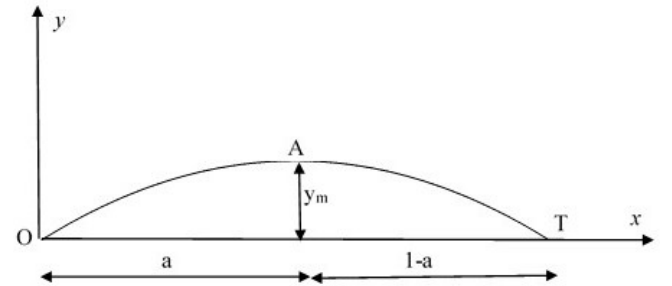
3.2 Far field boundary

The infinite physical domain surrounding the airfoil is truncated by an artificial boundary in the form of a circle whose centre is coincident with the leading edge of the airfoil. The diameter of the circle is chosen to be large enough so that it does not affect the results significantly. In order to find out a suitable position for the artificial boundary around the aerofoil such that the numerical boundary conditions imposed on it do not significantly affect the flow dynamics near the fixed aerofoil, numerical simulations are carried out on progressively smaller sized domains obtained by truncating a grid having the artificial boundary fixed at a dimensionless diameter of D = 120. A grid with 342,624 nodal points is then truncated at dimensionless diameters of 100, 80, 60, and 40 to yield five computational grids in all with identical grid sizes near the aerofoil. The minimum grid size near the aerofoil in both η and ξ directions for all the five cases is chosen as 10^{-4} which is smaller than the boundary layer thickness at most of the aerofoil surface. Therefore, it is expected that using this grid size captures the flow physics accurately and the results are not much deviated from the correct value. For each of these truncated grids, computation is performed for $M = 0.9$, $Re = 1.0 \times 10^6$ and $\alpha = 0°$, and the value of mean drag coefficient is compared as shown in Table 1.

Table 1   Variation of mean coefficient of drag with far field
boundary diameter

Diameter of the artificial boundary	Mean coefficient of drag
40	0.02215
60	0.02212
80	0.02207
100	0.02204
120	0.02202

The results obtained by varying the diameter of artificial
boundary around the aerofoil keeping all other parameters
constant tells us that there is very small variation in
the value of mean coefficient of drag as the diameter is
varied from 120 to 40. Therefore, it can be concluded
that any diameter beyond 40 is suitable for computation.
Nevertheless, to be extra careful we select the diameter of
far boundary as 80 for all our future computations.

The artificial boundary of the flow domain is divided
into two halves; the left half is defined as inflow and the
right half as outflow as shown in Figure 4.

Figure 4   Far field boundaries around the airfoil
(see online version for colours)
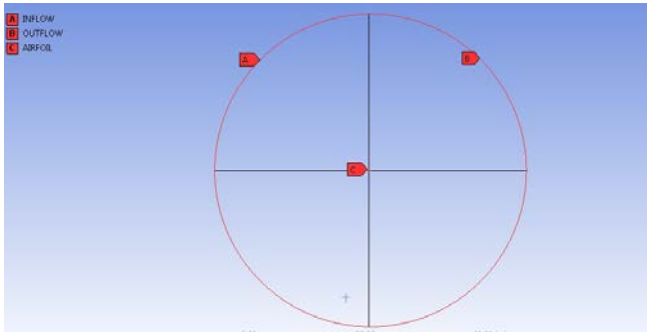
3.3   Grid structure

Multiblock structured mesh was generated using ICEM
CFD with proper clustering near the airfoil to capture
the flow physics appreciably. The total number of nodes
was 134,000 (425×315) with a minimum size of 10^{-4}
dimensionless units. Solutions were run with finer meshes
in order to ensure mesh independence. The finer meshes
were 150,000 with minimum size of 10^{-5} and 325,000
with minimum size of 10^{-4}. The maximum percentage
differences in lift, drag and moment coefficient is observed
to be less than 1% with much finer meshes. Therefore, the
results are considered to be mesh independent.

Table 2   Comparison of mean drag coefficient for different
grids

Grid	$N_\xi \times N_\eta$	No. of nodes	Minimum size	C_D
Grid 1	350×252	88,200	10^{-4}	0.0203
Grid 2	425×315	134,000	10^{-4}	0.0223
Grid 3	450×350	157,500	10^{-5}	0.0223
Grid 4	625×525	325,000	10^{-4}	0.0224

Figure 5   Pressure coefficient variation on the surface at
two grids (see online version for colours)
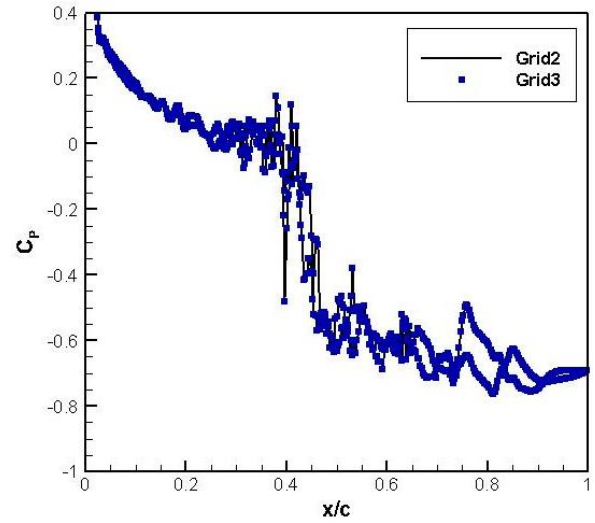
Figure 6   An O-mesh generated around the new cusped leading
edge airfoil, (a) farfield view (b) a view close to the
surface (see online version for colours)

(a)

(b)
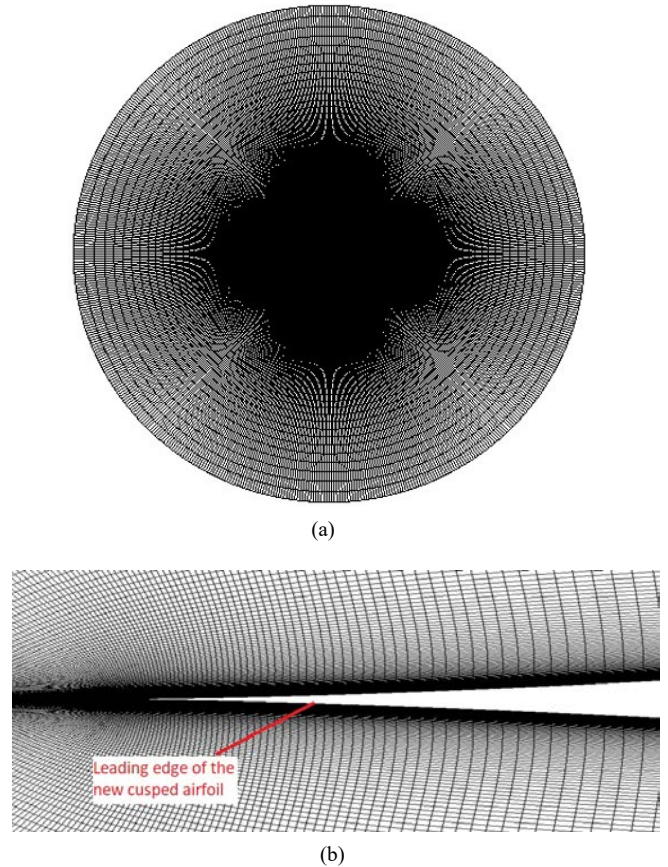
To assess the effects of grid resolution on the computed
results, computations are done on four different grids
keeping all other parameters constant $(M = 0.9,$
$Re = 1.0 \times 10^6$ and $\alpha = 0°)$ and the coefficient of drag
are compared. The results are summarised in Table 2.
Figure 5 shows the variation of C_P at the surface of the

airfoil at transonic conditions at two different grids. The results for other grids are intentionally dropped to clearly present the graph. Since, at transonic condition the surface of the airfoil is dominated by compression and expansion waves, lot of oscillations are visible in C_P plots. Despite severe oscillations, the values of pressure coefficient at grids 2 and 3 nearly overlap with each other. This justifies the choice of grid 2 at all the supersonic conditions at which the flow is much more stable and easier to solve. A typical grid with far boundary located at 80 m and near airfoil spacing of 10^{-4} m is shown in Figure 6.

3.4 Time step choice

Assessment of the effect of time step is performed by monitoring the results of flow past NACA 2S-(50)(03)-(50)(03) airfoil at M = 0.9, $\alpha = 0°$ at progressively smaller time steps. Initially, a dimensional time step of 5×10^{-3} s is taken and progressively reduced to $1 \times 10^{-3}s, 5 \times 10^{-4}s, 1 \times 10^{-4}s, 5 \times 10^{-5}s, 1 \times 10^{-5}s$ and $5 \times 10^{-6}s$ and the time histories of C_D and C_L are monitored. Upto time step size of 5×10^{-4} seconds, the solution could not proceed as Fluent showed divergence error. At time steps of 1×10^{-4} s and 5×10^{-5} s large number of iterations were required for the solution to converge at each time step. Moreover, the smaller the time step, the lesser is the amplitude of oscillation of the time histories. Since, no significant difference in the time histories and the number of iterations to converge at each time step is visible as time step is reduced from 1×10^{-5} s to 5×10^{-6} s, the time step size of 1×10^{-5} s is selected for all the future computations. The dimensional values of various time steps were converted into a non-dimensional time scale using the equation:

$$t = \frac{\bar{t}l}{U_\infty} \tag{18}$$

3.5 Validation

The validation of the various numerical procedures employed for computations is done by comparing the results obtained for NACA 2S-(50)(05)-(50)(05) with the experimental data of Mayer (1949) in terms of lift, drag and moment coefficients as shown in Table 3. The coefficient of pressure plots obtained from the current results is compared with the experimental data of Mayer (1949) in Figure 7, which demonstrates the accuracy of the methodology used for the present study. The pressure contour plots and streamlines for M = 1.85 and an angle of attack of 0°, 10° and 15° are shown in Figure 8. It is seen from these plots that the numerical schemes and different parameters employed in the present work quite nicely resolve the shock waves and other flow features. Moreover, the pressure coefficient plots are in good agreement with the experimental data. The slight deviation, especially at $\alpha = 15°$ for the lower surface, can be associated to the errors involved in discretisation, and specifically in resolving the shock strength of the strong shock attached to the lower surface. The data obtained from the present computations are in good agreement with the experimental data reported in Mayer (1949). The overall good agreement with the experimental data indicates that at a free stream Reynolds number $O(10^6)$, the choice of grid size, time step and other parameters appears to be appropriate for resolving the relevant flow features. Simulations are normally carried out for a minimum non-dimensional time of 300 units.

Table 3 Comparison of global flow parameters for NACA 2S-(50)(05)-(50)(05)

α (degrees)	M_∞	Present			Mayer (1949)		
		C_D	C_L	$C_{M,LE}$	C_D	C_L	$C_{M,LE}$
0	1.85	0.036	0.000	0.000	0.038	0.000	0.000
	2.13	0.029	0.000	0.000	0.030	0.000	0.000
10	1.85	0.118	0.445	0.174	0.121	0.445	0.169
	2.13	0.096	0.362	0.144	0.099	0.348	0.143
15	1.85	0.225	0.675	0.275	0.215	0.614	0.256
	2.13	0.189	0.569	0.233	0.188	0.548	0.228

Figure 7 Comparison of C_p profile for NACA 2S-(50)(05)-(50)(05) at M = 1.85 and an angle of attack of (a) $\alpha = 10°$ (b) $\alpha = 15°$

(a)   (b)
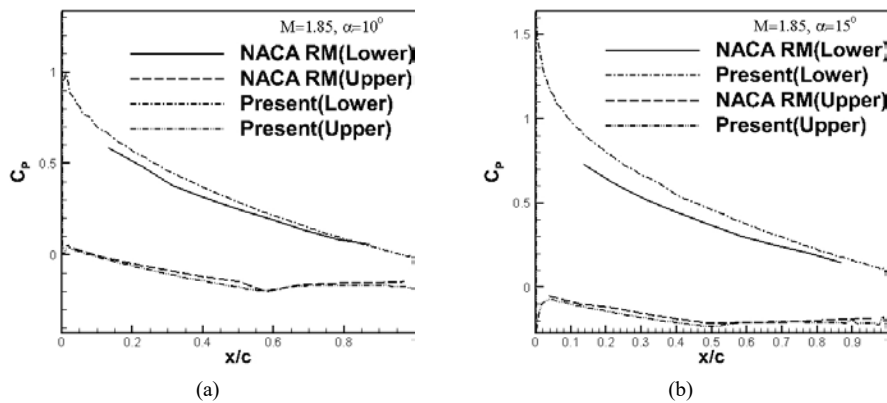
Figure 8   Flow features for NACA 2S-(50)(05)-(50)(05) at M = 1.85, (a) (b) (c) pressure contours (d) (e) (f) streamlines

(a)

(b)

(c)

(d)

(e)

(f)
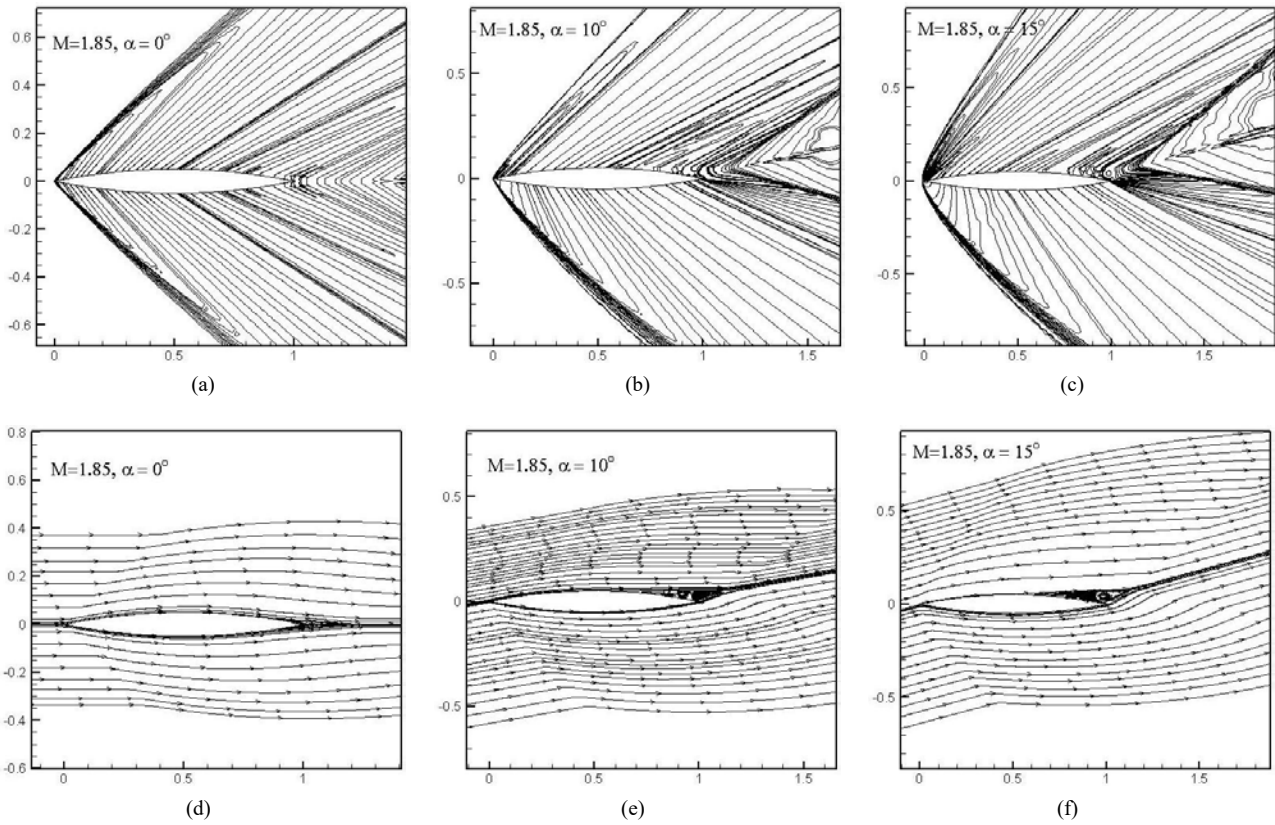
4   Results and discussion

This section is divided into two parts. In the first part, the aerodynamic parameters of the new cusped leading edge airfoil are compared with that of the conventional biconvex airfoil of same maximum thickness. After establishing the fact that the new airfoil is much superior than the conventional airfoil, the spatio-temporal dynamics of the new cusped leading edge airfoil are discussed in the second part.

4.1   Aerodynamic efficacy of the new cusped leading edge airfoil

4.1.1   Drag at cruise or no-lift condition ($\alpha = 0°$)

Table 4 shows the mean values of coefficient of drag of the cusped leading edge and the biconvex airfoils at $\alpha = 0°$. The percent change in the aerodynamic parameters defined as $\frac{(Parameter)_{cusped} - (Parameter)_{biconvex}}{(Parameter)_{biconvex}} \times 100$ is also calculated to highlight any potential benefits. It is readily observed that the present cusped leading edge shape of the supersonic airfoil has resulted in a large drag reduction of about 45% to 50% at $\alpha = 0°$ at all the supersonic Mach numbers. The reason behind this high drag reduction at supersonic Mach numbers is the mitigation or weakening of the shock waves formed at the leading edge. The value of deflection angle at the leading edge has been reduced from some finite value ($18°$) for the conventional

biconvex airfoil to zero by making the leading edge cusped as shown in Figure 9.

Table 4   Drag coefficient at $\alpha = 0°$

α (degree)	M	$<C_D>$ (cusped)	$<C_D>$ (biconvex)	$<\Delta C_D>$ (%)
0	1.25	0.035	0.068	–48.53
	1.50	0.025	0.050	–50.00
	1.85	0.019	0.036	–47.22
	2.13	0.016	0.029	–44.83

As per inviscid oblique shock wave theory, the deflection angle regulates shock angle and the strength of shock wave. The shocks always remain attached for a sharp wedge provided the deflection angle (not necessarily the wedge angle for non-zero angle of attack) is less than a critical (max.) value dependent on the incoming Mach number. In our case, the leading edge is cusped and hence has a zero deflection angle. Firstly, shocks are forming because the required deflection (equal to the angle of attack) still exists at the leading edge for the shock to form on the lower side of the airfoil. For zero angle of attack, due to formation of boundary layers, the outer inviscid flow does undergo a small deflection at the leading edge, thereby generating very weak shocks. In fact, this is a major reason for low drag at zero angle of attack.

Therefore, if the leading edge deflection angle is zero, the strong bow shock which is the main contributor of drag in supersonic flow might be converted into oblique

shock for a wider range of Mach number. To explore this, Mach contours and pressure coefficient profiles are plotted and shown in Figures 10, 11, 12 and 13 at Mach numbers of 1.25, 1.5, 1.85 and 2.13 respectively. In these figures, the left hand side [sub-figure (a)] shows the Mach contour on the new cusped leading edge airfoil, the middle one [sub-figure (b)] depicts the Mach contour on the biconvex airfoil and the right hand side [sub-figure (c)] compares the pressure variation on the two airfoils. At Mach 1.25, a much stronger bow shock is clearly visible for a biconvex airfoil in Figure 10(b). This results in a shoot up in the C_p value at the leading edge to about 1.5 [Figure 10(c)] resulting in a high wave drag (C_D of 0.068). Whereas, the value of C_p at the leading edge of the cusped airfoil is as low as 0.3 at Mach 1.25 [Figure 10(c)]. This is the result of a much weaker oblique shock formed at the leading edge of the cusped airfoil as depicted in Figure 10(a). Therefore, the wave drag is reduced drastically by about 48 % in the case of cusped airfoil (C_D of 0.035). An important point to be noted here is that since, both the airfoils are symmetric in nature, the pressure profiles are coinciding for the upper and the lower surfaces of the airfoils at $\alpha = 0°$. Another salient feature of the new airfoil design is that the location of maximum thickness has been shifted rear-side to about 0.75c. This has resulted in slightly higher pressure in the aft portion of the cusped airfoil as compared to the biconvex airfoil as is visible in Figure 10(c). But, as the wave drag is the major component of a supersonic flow drag which is significantly higher for the biconvex airfoil, a slight increase in pressure drag in the aft portion of the cusped airfoil does not have any noticeable effect.

Figure 9 Deflection angle
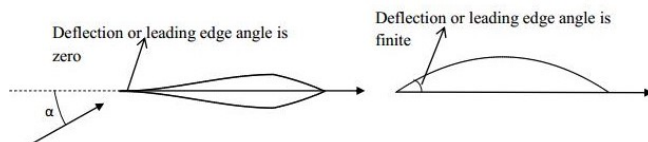
As the Mach number is increased to higher values, oblique shocks are formed even for the biconvex airfoil. But the oblique shock formed at the leading edge of cusped airfoil is much weaker in nature as compared to that formed on the biconvex airfoil. This again results in almost the same pressure profiles for the two airfoils. The value of C_p at the leading edge of biconvex airfoil shoots to around 1.6 at M = 1.50, 1.85 and 2.13. Whereas, C_p for the cusped airfoil stays around 0.25 at all the Mach numbers. Moreover, a higher pressure on the aft portion of the cusped airfoil is visible in all the above cases. Consequently, depending upon the flow condition, around 45 to 50 % drag reduction is achieved by the newly designed airfoil at all the Mach numbers investigated. Furthermore, the value of C_D is inversely proportional to the Mach number for both kinds of airfoils. But, the percentage change in drag follows a different trend as shown in Figure 14. In the range of Mach numbers investigated, the percentage change in drag initially increases and drops monotonously upto Mach 2.13 having its local maxima at Mach 1.5. It will be an

interesting future work to explore how this curve behaves if the Mach number is further increased.

4.1.2 Drag at high angle of attack ($\alpha = 10°$ and $\alpha = 20°$)

The values of drag coefficients for the two airfoils and the percentage difference in drag coefficient are computed at $\alpha = 10°$ and $\alpha = 20°$ and are mentioned in Table 5. At $\alpha = 10°$, detached bow shocks are formed at Mach 1.25 on both the airfoil as shown in the Mach contour plots in Figures 15(a) and 15(b). The standoff bow shock in case of the cusped airfoil is slightly stronger due to the sharp design of the leading edge. This results in a higher pressure on the lower surface of the cusped airfoil as is visible in the C_p plot in Figure 15(c). Consequently, the new cusped design of the airfoil is leading to about 5 % higher wave drag as compared to the biconvex airfoil. However, as the free stream velocity is increased to Mach 1.5, the shock waves move closer to the airfoil as shown in Figures 16(a) and 16(b). Since the deflection angle is zero for the cusped airfoil, an oblique shock appears attached to the leading edge. Whereas, for the finite deflection angled biconvex airfoil, although close to the leading edge, but a stronger bow shock is visible. Therefore, a higher pressure is developed near the leading edge of the biconvex airfoil [Figure 16(c)]. But the curvature of the cusped airfoil leads to higher pressure on the aft portion as in the previous cases. This balances the high pressure zone and results in equal drag for both the airfoils at M = 1.5. Moreover, at higher Mach numbers of M = 1.85 and M = 2.13, oblique shocks are formed on both the airfoils. It is found that the oblique shock in case of new airfoil is much weaker in strength than for the biconvex airfoil due to the same reason as stated for $\alpha = 0°$ (Figures 17 and 18). This results in a lesser pressure near the leading edge on both the upper and lower surfaces of the cusped airfoil as shown in the C_p plots [Figures 17(c) and 18(c)]. Therefore, a drag reduction of about 18 % and 16 %, at Mach 1.85 and 2.13 respectively, is achieved by using the new cusped leading edge airfoil at $\alpha = 10°$.

As the angle of attack is further increased to $\alpha = 20°$, the lower limit of Mach number at which drag reduction is achieved increases to above 2.0. Below this speed, the new airfoil produces a much higher drag as compared to the conventional biconvex airfoil. The reason behind this behaviour of the new airfoil is same as explained for the case of $\alpha = 10°$. As the angle of attack is quite high, the speed upto which detached bow shocks are formed increases to about Mach 2.0. Since stronger bow shocks are formed in case of cusped leading edge airfoil, the pressure developed over the surface is more as compared to biconvex airfoil. Hence, the new airfoil has larger drag up to Mach 2.0. As Mach number is increased beyond this value, attached oblique shocks are formed resulting in drag reduction. The Mach contours and C_p plots are not shown intentionally to avoid repetition, as they are similar in nature as for the case of $\alpha = 10°$.

Figure 10   Comparison of flow dynamics for $\alpha = 0°$ and M = 1.25 (see online version for colours)

(a)   (b)   (c)
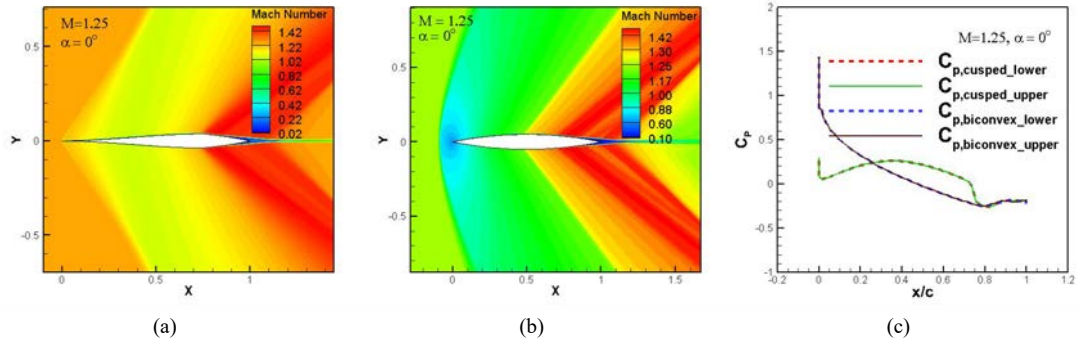
Figure 11   Comparison of flow dynamics for $\alpha = 0°$ and M = 1.50 (see online version for colours)

(a)   (b)   (c)
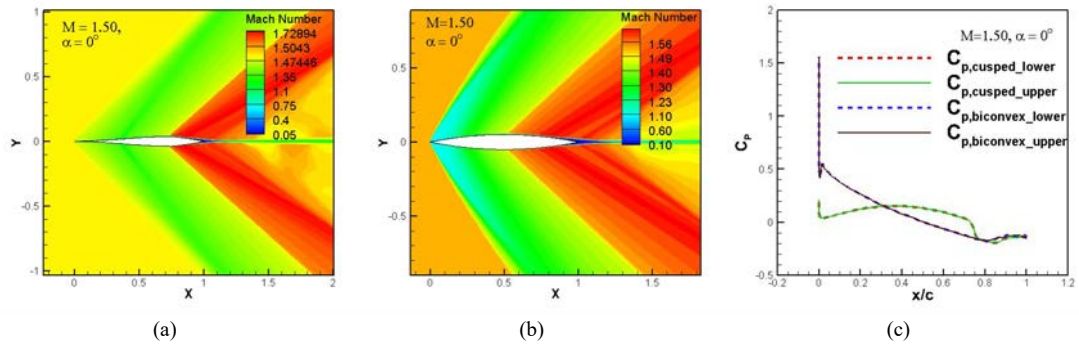
Figure 12   Comparison of flow dynamics for $\alpha = 0°$ and M = 1.85 (see online version for colours)

(a)   (b)   (c)
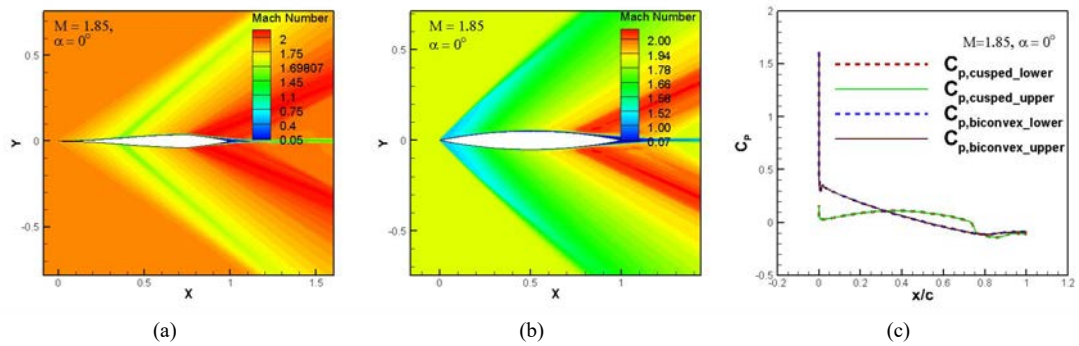
Figure 13   Comparison of flow dynamics for $\alpha = 0°$ and M = 2.13 (see online version for colours)

(a)   (b)   (c)
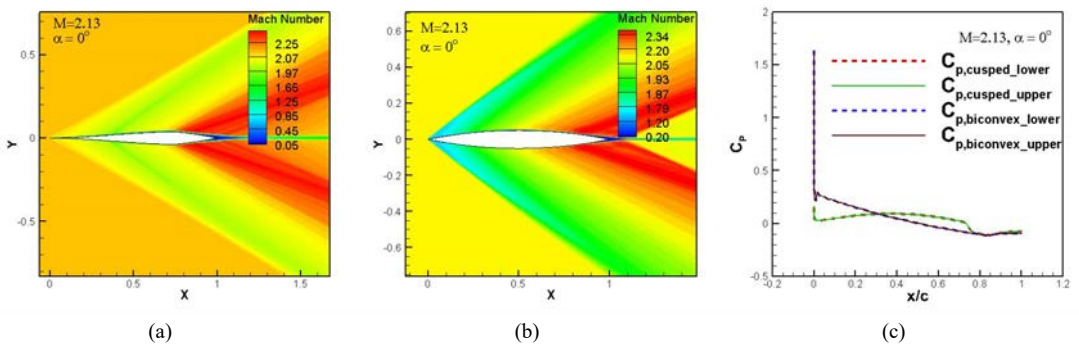
Figure 14 Drag reduction vs. Mach number (see online version for colours)

Table 6 Comparison of lift coefficient of the cusped airfoil with that of NACA 2S-(50)(05)-(50)(05)

α (degree)	M	$<C_L>$ (cusped)	$<C_L>$ (biconvex)	$<\Delta C_L>$ (%)
10	1.25	0.829	0.702	18.09
	1.50	0.689	0.585	17.78
	1.85	0.435	0.445	–2.25
	2.13	0.357	0.362	–1.38
20	1.25	1.196	1.169	2.31
	1.50	1.113	1.061	4.90
	1.85	0.967	0.691	39.94
	2.13	0.780	0.687	13.54
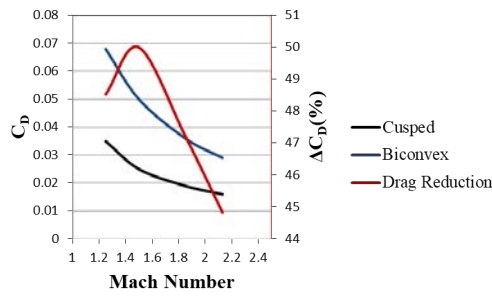
Table 5 Drag coefficient at $\alpha = 10°$ and $\alpha = 20°$

α (degree)	M	$<C_D>$ (cusped)	$<C_D>$ (biconvex)	$<\Delta C_D>$ (%)
10	1.25	0.181	0.172	5.23
	1.50	0.153	0.153	0.00
	1.85	0.096	0.118	–18.64
	2.13	0.080	0.096	–16.67
20	1.25	0.473	0.473	0.00
	1.50	0.439	0.431	1.86
	1.85	0.383	0.312	22.76
	2.13	0.307	0.311	–1.29

Table 7 Lift to drag ratio

α (degrees)	M	$(L/D)_{cusped}$	$(L/D)_{biconvex}$	$\Delta(L/D)$(%)
10	1.25	4.58	4.08	12.25
	1.50	4.50	3.82	17.80
	1.85	4.53	3.77	20.16
	2.13	4.46	3.77	18.30
20	1.25	2.53	2.47	2.43
	1.50	2.54	2.46	3.25
	1.85	2.52	2.21	14.03
	2.13	2.54	2.21	14.93

4.1.3 Lift

Since the airfoils considered for the present study are symmetric, the pressure developed at $\alpha = 0°$ on top and bottom surfaces are exactly equal as indicated in Figures 10(c), 11(c), 12(c) and 13(c) at various Mach numbers. Therefore, no lift is generated at $\alpha = 0°$. As soon as some angle of attack is provided, finite lift is generated due to the formation of stronger shocks on the lower surface resulting in higher pressure (Figures 15 to 18). Moreover, flow separation zones created on the upper surface of the airfoil also contributes to lift. The details of flow separation and vortices will be discussed separately in later sections. The values of lift coefficients at $\alpha = 10°$ and $\alpha = 20°$ calculated from the results are listed in Table 6. Since stronger detached bow shocks are formed at the lower surface of the cusped leading edge airfoil at low supersonic Mach numbers as discussed above, lift enhancement is achieved at $\alpha = 10°$ and $\alpha = 20°$. At high Mach numbers, attached oblique shocks are formed at the leading edge. As weaker oblique shocks are formed in case of new airfoil at $\alpha = 10°$, a slight decrease in lift is observed at high supersonic Mach numbers (M = 1.85 and M = 2.13). In the case of $\alpha = 20°$, at all the Mach numbers a higher lift is generated by the cusped airfoil because of the stronger bow shocks due to the sharp edged design. The maximum value of lift at $\alpha = 20°$ is achieved at Mach 1.85 as the strongest bow shock appears at this Mach number. Nevertheless, lift to drag ratio of the new cusped leading edge airfoil is always greater than that of the conventional biconvex circular-arc airfoil at all supersonic flight conditions as illustrated in Table 7.

4.1.4 Pitching moment

Along with lift and drag, an important global flow parameter which plays crucial role in determining the longitudinal static stability of the airfoil is pitching moment coefficient. For the present investigation, moment coefficients for all the cases are determined about the leading edge and reported in Table 8. The counter clockwise direction is considered as positive. Since, the line of action passes through the aerodynamic centre at $\alpha = 0°$, the pitching moment is zero and thus C_M at $\alpha = 0°$ is not reported here.

The table shows that the moment of the new airfoil is much higher (10–20%) than the biconvex airfoil for all the cases of supersonic flow at $\alpha = 10°$. This shows that the new airfoil is more stable than the conventional biconvex airfoil in supersonic flow regime at $\alpha = 10°$ for clockwise forces or disturbances in α. But the new airfoil is less stable as counterclockwise forces are acted upon it. It is also found that the new airfoil is slightly more stable to clockwise disturbances at $\alpha = 20°$ in high supersonic flow regime as the values of C_M are higher by an amount of 7–10% at M = 1.85 and M = 2.13. The static stability of the new airfoil in supersonic flow regime is further confirmed by C_M versus α plot in Figure 19. Figure 19 demonstrates that the slope of the cusped airfoil is always higher than the biconvex airfoils at the corresponding Mach number. This means that the new airfoil develops higher counter-clockwise torque. As a result, it can resist to more clockwise aerodynamic forces and hence is more stable. But a slight counter-clockwise disturbance may lead to higher instability.

Figure 15   Comparison of flow dynamics for $\alpha = 10°$ and M = 1.25 (see online version for colours)

(a)   (b)   (c)
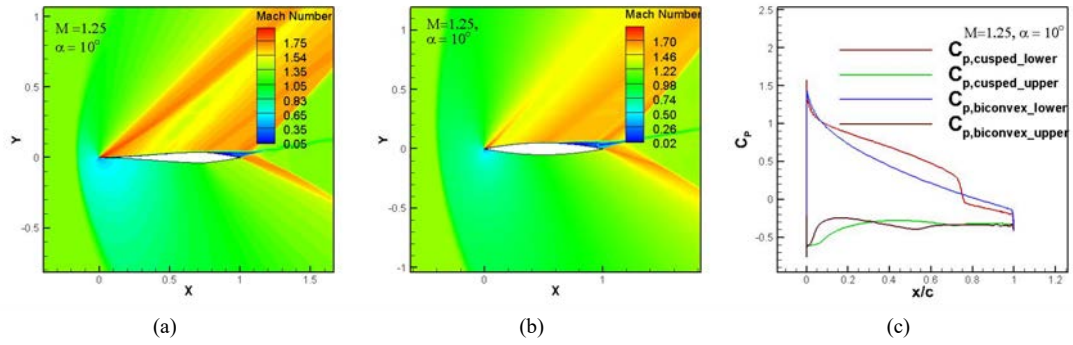
Figure 16   Comparison of flow dynamics for $\alpha = 10°$ and M = 1.50 (see online version for colours)

(a)   (b)   (c)
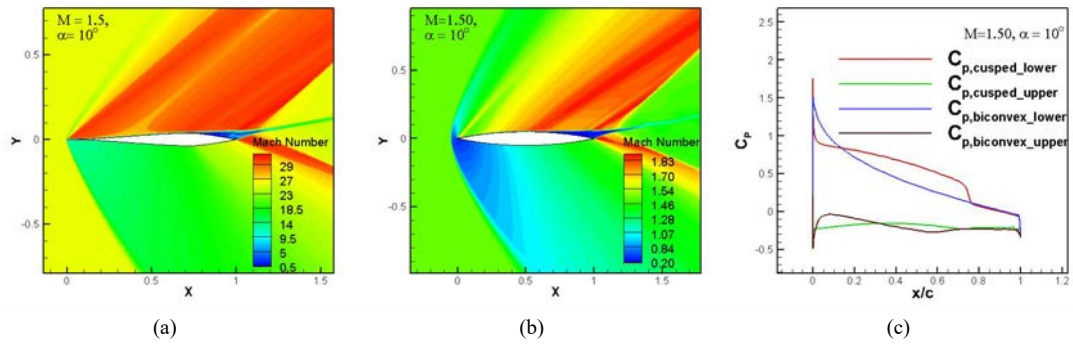
Figure 17   Comparison of flow dynamics for $\alpha = 10°$ and M = 1.85 (see online version for colours)

(a)   (b)   (c)
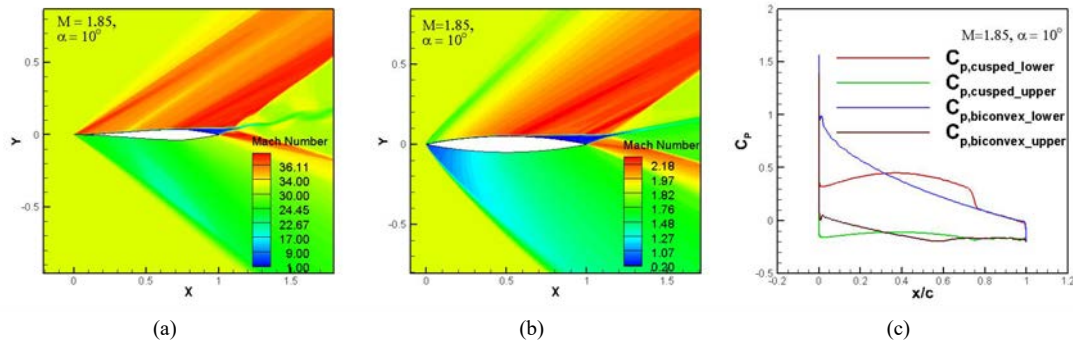
Figure 18   Comparison of flow dynamics for $\alpha = 10°$ and M = 2.13 (see online version for colours)

(a)   (b)   (c)
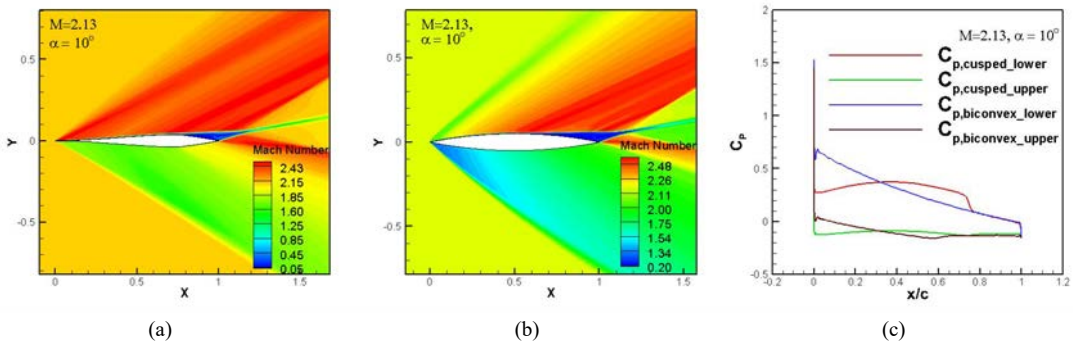
Figure 19 Comparison of pitching moment coefficient versus angle of attack for the new airfoil with that of conventional biconvex airfoil at various free stream Mach numbers

(a)

(b)

(c)

(d)
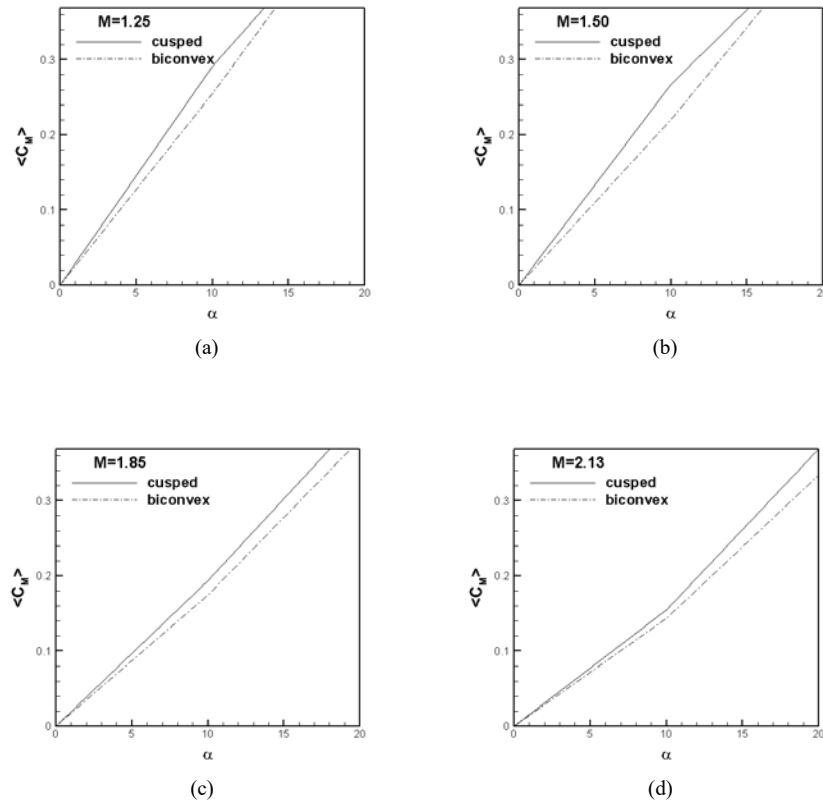
Table 8 Pitching moment coefficient

α (degree)	M	$<C_M>$ (cusped)	$<C_M>$ (biconvex)	$<\Delta C_M>$ (%)
10	1.25	0.292	0.255	14.5
	1.50	0.267	0.221	20.8
	1.85	0.194	0.175	10.9
	2.13	0.155	0.144	7.64
20	1.25	0.519	0.530	–2.07
	1.50	0.467	0.466	0.21
	1.85	0.412	0.382	7.85
	2.13	0.369	0.334	10.5

4.1.5 Fluctuations in aerodynamic forces

The fluctuations in the aerodynamic forces about the mean value should be minimum for a relatively smooth flight. The root-mean-square (rms) values of the global flow parameters of the new airfoil are compared with that of a conventional biconvex airfoil of same maximum thickness in Table 9. The unsteadiness in supersonic flow past the cusped leading edge airfoil at $\alpha = 0°$ (if at all) is of very small magnitude of the order of 10^{-4}. Therefore, the rms values at $\alpha = 0°$ in supersonic flow regime are zero for most of the cases (upto 4 decimal places) and do not pose a concern. As the angle of attack is increased to higher values ($\alpha = 10°$ and $\alpha = 20°$), higher rms values are observed in most of the cases in comparison to those for the biconvex airfoil. But the differences in the rms values are of small magnitude. Hence, the fluctuations of aerodynamic forces do not pose any serious concern of hindering the supersonic flight at high angles of attack.

4.2 Spatio-temporal flow dynamics

In order to understand the flow dynamics of the new cusped leading edge airfoil at different supersonic flow conditions, the spatial flow patterns as represented by instantaneous streamlines, pressure contours and Mach contours are generated. The surface distribution over the airfoil is demonstrated in the form of coefficient of pressure and skin friction coefficient plots. The temporal dynamics are presented by the time histories of global flow parameters such as coefficient of drag and coefficient of lift.

Figures 20 to 23 illustrate the spatial flow patterns at $\alpha = 0°$ for different Mach numbers. The streamline patterns show that at all the supersonic Mach numbers, the flow is completely attached to both the upper and lower surfaces of the airfoil with only a small separation region near the trailing edge. Very small scale counter rotating vortices are formed in the wake region of the airfoil. The flow is smooth and passes over the airfoil in the absence of any strong shock wave. The pressure contours and Mach contours depicts the formation of a weak shock wave at the leading edge of the airfoil and no strong oblique shock wave is formed as in the case of biconvex circular-arc

airfoil. The pressure contour plot depicts a low pressure region beyond the point of maximum thickness (0.75c) with the formation of expansion waves at both the upper and the lower surfaces of the airfoil. Since the surface of the airfoil turns away from the direction of flow at the point of maximum thickness, expansion waves are formed at this point. To regain the free stream pressure, compression shocks are created in the wake of the airfoil. Moreover, it is observed that as the free stream Mach number is increased, the shock wave gets more flattened.

The surface distribution of coefficient of pressure and skin friction coefficient over the cusped leading edge airfoil at $\alpha = 0°$ for different supersonic Mach numbers are shown in Figures 24 to 27. The pressure distribution and the skin friction coefficient are exactly same on the top and bottom surfaces of the airfoil because the airfoil is symmetric about the chord line and the flow is horizontal. As the leading edge is a stagnation point, a high pressure and a very high skin friction coefficient is visible which sharply dips down to a low value for all the cases. The pressure again rises gradually to a higher value owing to the gradual compression over the concave portion in the front half of the airfoil. As the flow traverses the convex portion, the flow accelerates and the pressure starts to fall initially gradually and rather sharp as it negotiates the maximum thickness location. The skin friction coefficient remains nearly constant and close to zero all over the airfoil. It becomes negative at about 0.9c which is the point of flow separation as stated above.

Figures 28 to 31 show the time histories of the global flow parameters namely coefficient of drag and coefficient of lift. The values of coefficient of drag are quite low for all the cases as the body is streamlined with weak shock formation. Moreover, the shape of the airfoil is such that low pressure exists over a large part of the airfoil. It is also observed that as the Mach number is increased, the value of C_D decreases. There is no lift generation at an angle of attack of 0° because the pressure distribution is exactly the same on the upper and lower surfaces of the airfoil due to its symmetry about the chord line. The time histories of C_D show a steady value for all the cases whereas that of C_L shows a periodic unsteadiness of the order of 10^{-4} at low supersonic Mach numbers. The dimensionless

frequency of the time history of C_L at M = 1.25 is 0.8. The reason behind this periodic unsteadiness are the unsteady vortices formed in the wake of the airfoil. These vortices are changing their structures with time and causing the solution to be slightly unsteady. As the Mach number is increased, the time history of C_L becomes steady.

Since the leading edge of the airfoil is sharp and pointed, the flow is expected to separate as soon as some angle of attack is provided; but an unusual flow is seen at the leading edge of the airfoil at $\alpha = 10°$. The flow is completely attached to the airfoil and a close look at the leading edge (Figure 32) shows localised flow separation and very small scale vortex formation in a tiny region on the upper surface near the leading edge at M = 1.25. This localised flow separation region is eliminated as the Mach number is increased. The flow attachment to the airfoil can be attributed to the formation of strong shock and expansion waves at the leading edge. The flow takes a sharp turn due to the formation of shock and expansion waves and the fluid is forced to remain attached to the airfoil. A small separation region also exists on the upper surface near the trailing edge with the formation of small scale trapped vortices as shown in Figures 33 to 36. These vortices are trapped owing to the formation of shock wave at the trailing edge and expansion wave at the point of maximum thickness.

The pressure contours and Mach contours in Figure 33 show the formation of a bow shock at a distance of about 16 cm from the leading edge at M = 1.25. The shock wave moves closer to the airfoil as the Mach number is increased and eventually attached oblique shocks are formed at Mach 1.5 and beyond (Figures 34, 35 and 36). It is observed that a strong attached oblique shock is formed only at the lower surface at higher Mach numbers. Whereas, expansion waves are observed at the leading edge over the top surface in all the cases. The expansion waves are formed as the flow negotiates the sharp leading edge and moves over the top surface. Expansion waves at the point of maximum thickness at the lower surface and compression shocks in the wake region are observed in all the cases of supersonic flow at $\alpha = 10°$.

Table 9 Comparison of rms values of the aerodynamic forces

α (degrees)	M	$C_{D,rms}$ (cusped)	$C_{D,rms}$ (biconvex)	$C_{L,rms}$ (cusped)	$C_{L,rms}$ (biconvex)	$C_{M,rms}$ (cusped)	$C_{M,rms}$ (biconvex)
0	1.25	0.0000	0.0000	0.0001	0.0004	0.0001	0.0004
	1.50	0.0000	0.0000	0.0000	0.0000	0.0000	0.0000
	1.85	0.0000	0.0000	0.0000	0.0000	0.0000	0.0000
	2.13	0.0000	0.0000	0.0000	0.0000	0.0000	0.0000
10	1.25	0.0000	0.0000	0.0000	0.0000	0.0000	0.0000
	1.50	0.0003	0.0001	0.0008	0.0003	0.0007	0.0003
	1.85	0.0002	0.0000	0.0006	0.0000	0.0005	0.0000
	2.13	0.0000	0.0000	0.0001	0.0000	0.0001	0.0000
20	1.25	0.0006	0.0000	0.0008	0.0000	0.0016	0.0000
	1.50	0.0000	0.0008	0.0000	0.0014	0.0000	0.0014

Figure 20 Flow features at $\alpha = 0°$ and M = 1.25, (a) streamlines (b) pressure contours (c) Mach contours (see online version for colours)

(a)　　　　　　　　　　　(b)　　　　　　　　　　　(c)
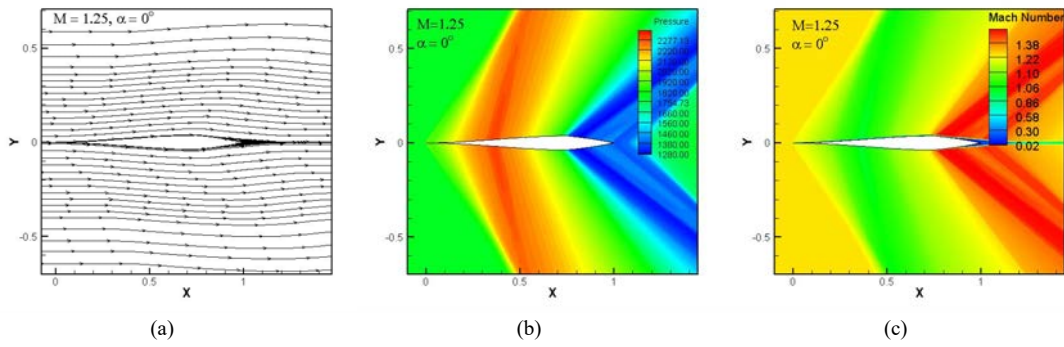
Figure 21 Flow features at $\alpha = 0°$ and M = 1.50, (a) streamlines (b) pressure contours (c) Mach contours (see online version for colours)

(a)　　　　　　　　　　　(b)　　　　　　　　　　　(c)
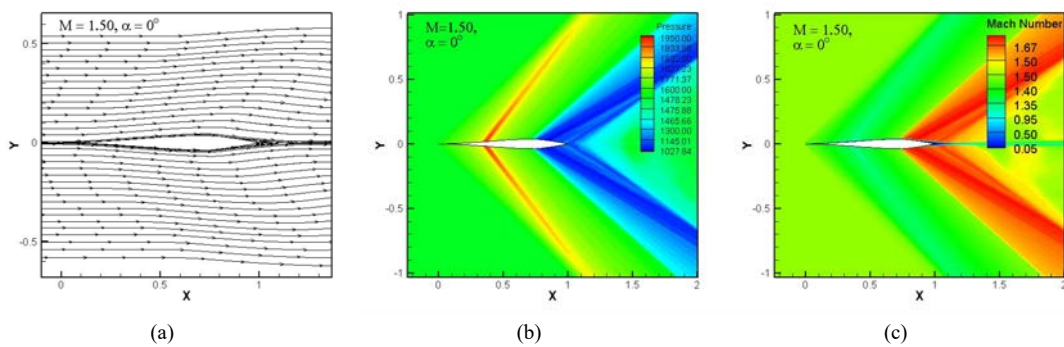
Figure 22 Flow features at $\alpha = 0°$ and M = 1.85, (a) streamlines (b) pressure contours (c) Mach contours (see online version for colours)

(a)　　　　　　　　　　　(b)　　　　　　　　　　　(c)
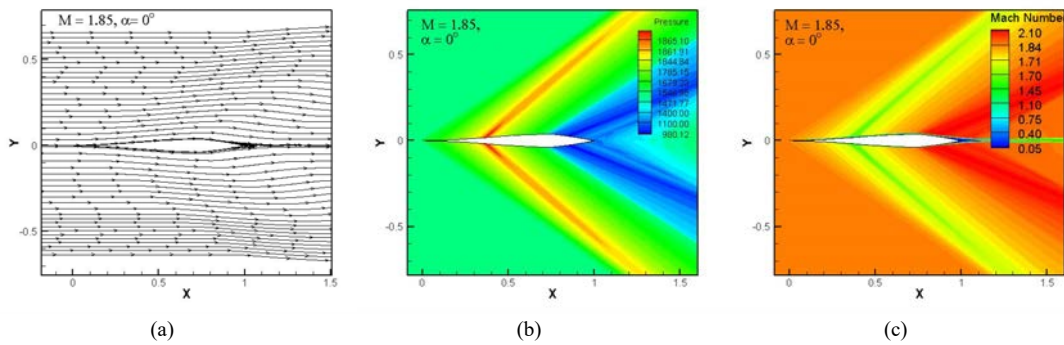
Figure 23 Flow features at $\alpha = 0°$ and M = 2.13, (a) streamlines (b) pressure contours (c) Mach contours (see online version for colours)

(a)　　　　　　　　　　　(b)　　　　　　　　　　　(c)
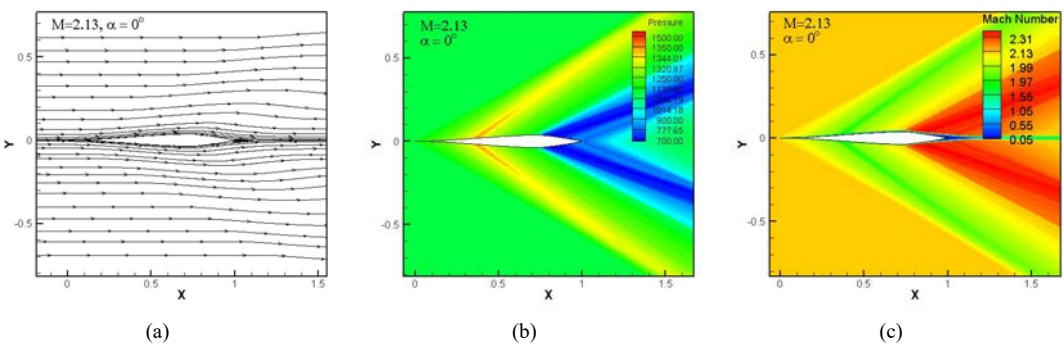
Figure 24 Pressure coefficient (C_P) and skin friction coefficient (C_f) plots at $\alpha = 0°$ and M = 1.25

(a)   (b)
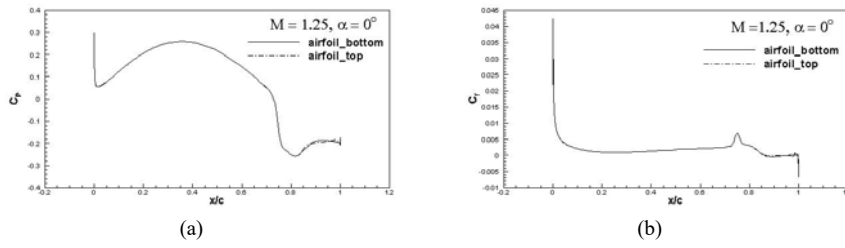
Figure 25 Pressure coefficient (C_P) and skin friction coefficient (C_f) plots at $\alpha = 0°$ and M = 1.50

(a)   (b)
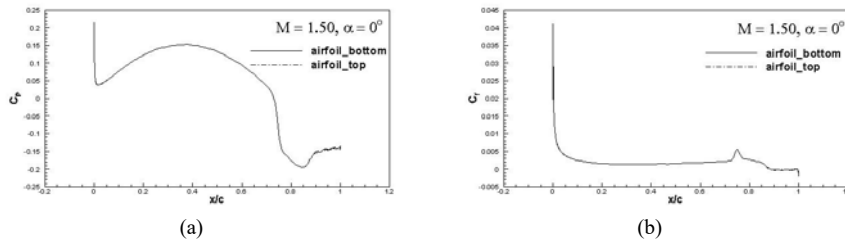
Figure 26 Pressure coefficient (C_P) and skin friction coefficient (C_f) plot at $\alpha = 0°$ and M = 1.85

(a)   (b)
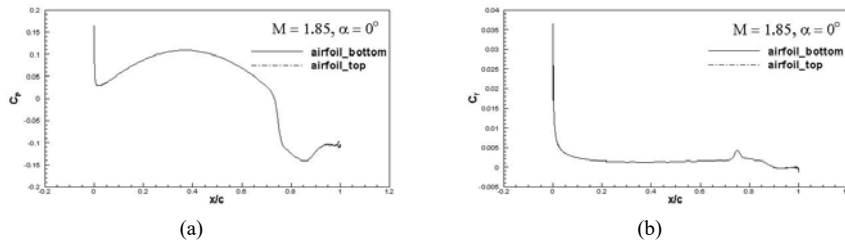
Figure 27 Pressure coefficient (C_P) and skin friction coefficient (C_f) plot at $\alpha = 0°$ and M = 2.13

(a)   (b)
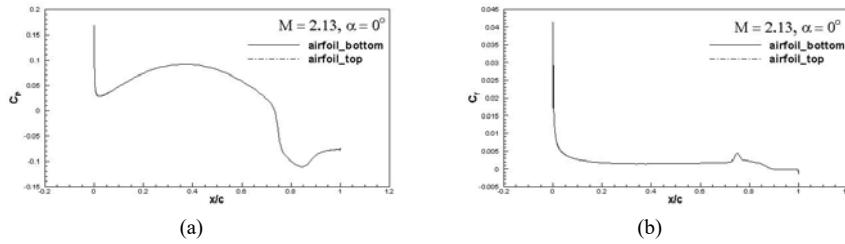
Figure 28 Time histories of drag and lift coefficients at $\alpha = 0°$ and M = 1.25

(a)   (b)
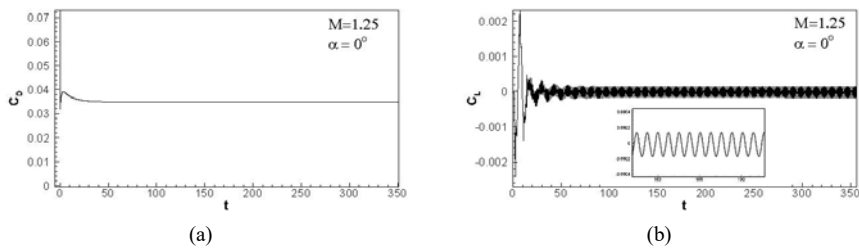
Figure 29 Time histories of drag and lift coefficients at $\alpha = 0°$ and M = 1.50

(a)

(b)
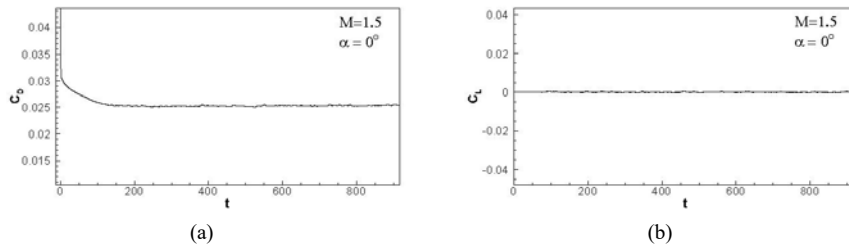
Figure 30 Time histories of drag and lift coefficients at $\alpha = 0°$ and M = 1.85

(a)

(b)
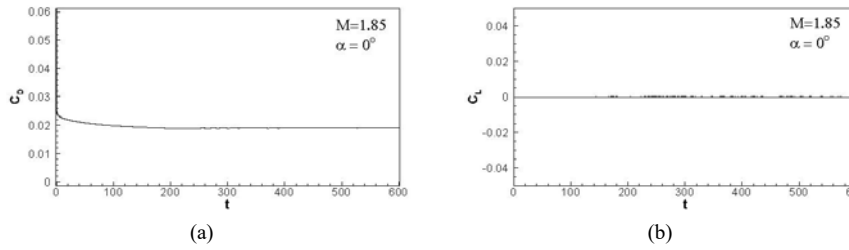
Figure 31 Time histories of drag and lift coefficients at $\alpha = 0°$ and M = 2.13

(a)

(b)
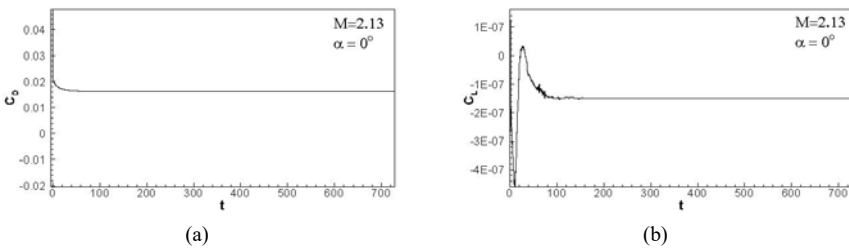
Figure 32 A zoomed view of the flow at the leading edge of the new cusped leading edge airfoil at M = 1.25 and $\alpha = 10°$
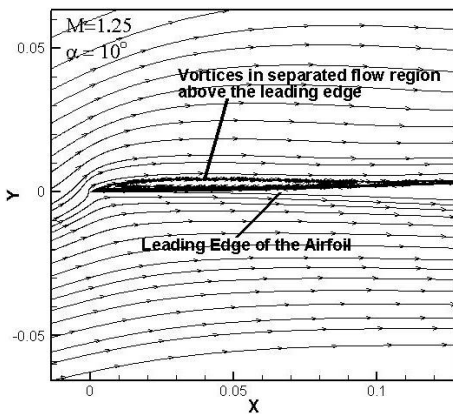
Figures 37 to 40 show the coefficient of pressure and skin friction coefficient plots for different supersonic Mach numbers at $\alpha = 10°$. It is observed that a high pressure exists at the lower surface of the airfoil near the leading edge which slowly decreases and reaches a low value at about 0.75c (the point of maximum thickness) while low pressure exists at the upper surface and remains almost constant all along the airfoil at Mach 1.25 and Mach

1.50. Whereas at higher Mach numbers (M = 1.85 and M = 2.13), after an initial sudden decrement, the pressure again rises gradually to a higher value owing to the gradual compression over the concave portion in the front half of the airfoil. As the flow traverses the convex portion, the flow accelerates and the pressure starts to fall initially gradually and rather sharp as it negotiates the maximum thickness location. Although the high pressure near the leading edge due to the formation of strong shock may lead to high wave drag, the large pressure difference between the upper and lower surfaces provides handsome amount of lift at the above conditions.

The value of C_f is negative (Figure 37) in the vicinity of the leading edge at the upper surface which is an indication of a small flow separation region with vortex formation as explained above for M = 1.25. As the Mach number is increased, this flow separation zone disappears and therefore there is a shoot-up in the value of C_f at Mach 1.50, 1.85 and 2.13. The flow separation on the upper surface at the point of maximum thickness is characterised by negative value of C_f for all the cases of supersonic flow at $\alpha = 10°$. A high value of C_f on the lower surface at the trailing edge and a slight bump at about 0.75c on the lower surface are depicted in the C_f plots at all the Mach numbers. This may be due to the fluid particles undergoing

acceleration around these points owing to the curvature, resulting in high skin friction.

The time histories of global flow parameters for different Mach numbers at $\alpha = 10°$ are shown in Figures 41 to 44. Since detached bow shock is formed at low Mach numbers, there exists a high pressure zone just before the leading edge. Therefore, high value of coefficient of drag is seen at M = 1.25 as compared to the other cases. However, at all the Mach numbers investigated, the value of coefficient of lift is significantly high as large pressure differences are created on the upper and the lower surfaces. The lift-drag ratio (L/D) is around 4.58 at M = 1.25. As the free stream Mach number is increased to higher values attached weaker oblique shocks are formed as explained above. Therefore, the drag decreases with an increase in Mach number. The value of lift also shows a decreasing trend with an increase in free stream Mach number. The time histories show that the flow is steady at M = 1.25. The flow becomes unsteady with multiple frequencies as the Mach number is increased. The power spectral distribution of the time histories of C_D and C_L at M = 1.50 and M = 1.85 are shown in Figure 45. At M = 1.5, the spectral analysis shows a broadband spectrum with the dominant dimensionless frequencies in the range of 0.095 to 0.384 for both C_D and C_L. After this range the power becomes very small of the order of 10^{-4} and the frequencies can be attributed to numerical errors or noise. The power spectrum at M = 1.85 depicts the dominant dimensionless frequencies as $f_1 = 0.20, f_2 = 0.28$ and $f_3 = 0.12$ for both C_D and C_L. As the Mach number is further increased to M = 2.13 a periodic solution with a dimensionless frequency of 2.0 for both C_D and C_L is observed. It is interesting to observe that the magnitude of unsteadiness for all the cases of supersonic flow at $\alpha = 10°$ is very small of the order of 10^{-3} to 10^{-4}.

Figure 46 shows the spatial patterns of the supersonic flow past the new cusped leading edge airfoil at $\alpha = 20°$ and Mach 1.25. Since the angle of attack is quite high, the flow gets completely separated at the upper surface with large scale vortex formation at low supersonic Mach numbers as shown in the streamline patterns at M = 1.25. The flow remains attached to the lower surface. The pressure contours at M = 1.25 depict the formation of detached bow shock at a distance of about 1.15 m before the leading edge of the airfoil. Shocks are also created in the wake region of the airfoil. The zoomed view of Mach contour at M = 1.25 shows the possible formation of slip lines. This is further confirmed by extracting the flow field data along a line $x/c = 0.3$ and then generating the plots of tangential velocity, density and temperature across the slip surface as shown in Figure 47. The sharp jump in tangential velocity, temperature and density as we move away from the airfoil surface establishes the fact that a slip line exists close to the upper surface of the airfoil.

The contour plots in Figures 48, 49 and 50 show that as the Mach number is increased the bow shock moves closer to the leading edge and eventually attached oblique shocks are formed at higher Mach numbers. At M = 1.50 the distance of bow shock is about 23 cm from the leading edge while it becomes as low as 2 cm at M = 1.85. As the free stream Mach number is further increased to 2.13 attached oblique shocks are observed only at the lower surface while expansion waves are formed at the upper surface. Expansion waves are also formed at the leading edge of the upper surface along with detached shock waves at Mach 1.50 and 1.85. These expansion waves form as the flow negotiates the sharp leading edge and moves over the top surface. Expansion waves at the point of maximum thickness at the lower surface and compression shocks in the wake region are observed in all the cases of supersonic flow at $\alpha = 20°$. The streamline patterns show that the stagnation point is formed on the lower surface with flow moving on either side of the stagnation point. Further moving from the stagnation point around the leading edge, the flow undergoes separation right from the leading edge itself at low supersonic Mach numbers. As the shock moves closer to the airfoil at M = 1.50, only localised flow separation region exists at the leading edge which extends up to a few percent of the chord as illustrated in the zoomed view of the leading edge in Figure 51. The fluid after reattaching and flowing along the upper surface again separates at the point of maximum thickness with the formation of trapped vortices near the trailing edge. The flow separation at the leading edge is completely eliminated as the Mach number is further increased. At M = 1.85 and M = 2.13, flow separation region exists only in the vicinity of the trailing edge. The Mach contours at M = 1.50, M = 1.85 and M = 2.13 shows the possible formation of slip lines near the trailing edge. This is further confirmed by extracting the flow field data along a line $x/c = 0.8$ and then generating the plots of tangential velocity, density and temperature across the slip surfaces as demonstrated in Figures 52, 53 and 54.

Moreover, since there is a large gap between the bow shock wave and the airfoil, high pressure region exists ahead of the airfoil at low supersonic speeds. Therefore, the C_P plot at M = 1.25 in Figure 55 shows a high pressure on the lower surface at the leading edge which slowly decreases. Since there is complete flow separation on the upper surface at M = 1.25, the C_P plot shows a very low pressure which remains nearly constant all along the upper surface. At M = 1.50 and M = 1.85 in Figures 56 and 57 respectively, high pressure at the lower surfaces is owing to the formation of stagnation point. As localised flow separation region exists at the leading edge at M = 1.50, low pressure is observed which increases gradually as the flow reattaches. A sharp decrease in C_P at the point of maximum thickness is seen in all the cases. This can be attributed to the sudden discontinuity in the airfoil at that point and the formation of Prandtl Mayer expansion waves. At M = 2.13, the formation of strong oblique shock at the leading edge of the lower surface leads to high pressure as illustrated in Figure 58.

Figure 33 Flow features at $\alpha = 10°$ and M = 1.25, (a) streamlines (b) pressure contours (c) Mach contours (see online version for colours)

(a)

(b)

(c)
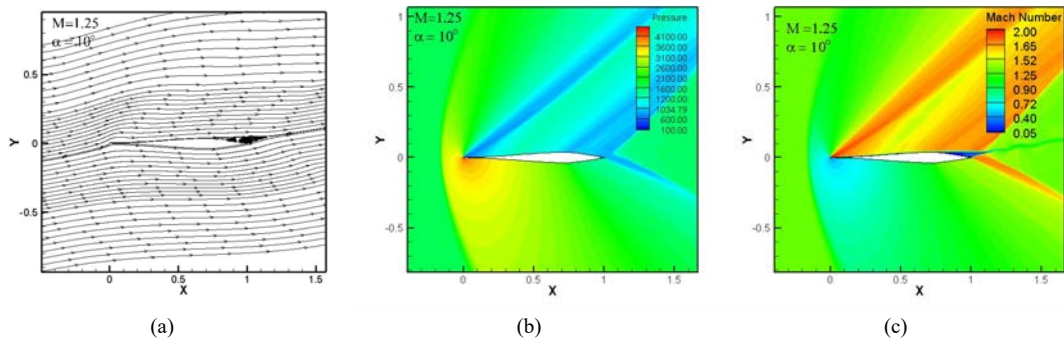
Figure 34 Flow features at $\alpha = 10°$ and M = 1.50, (a) streamlines (b) pressure contours (c) Mach contours (see online version for colours)

(a)

(b)

(c)
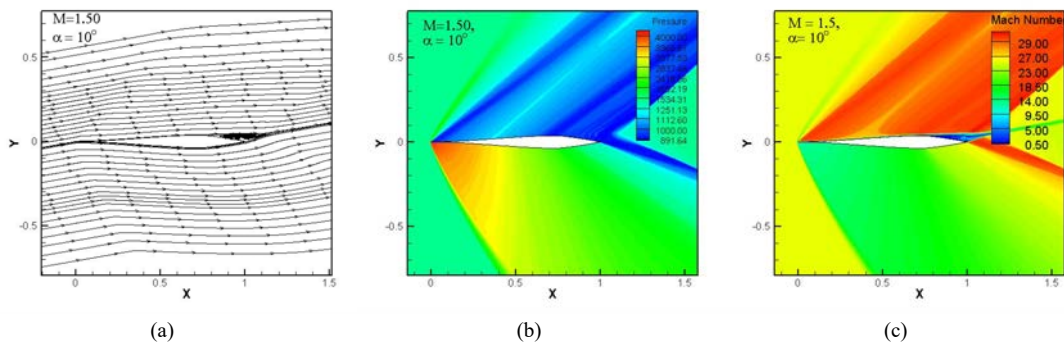
Figure 35 Flow features at $\alpha = 10°$ and M = 1.85, (a) streamlines (b) pressure contours (c) Mach contours (see online version for colours)

(a)

(b)

(c)
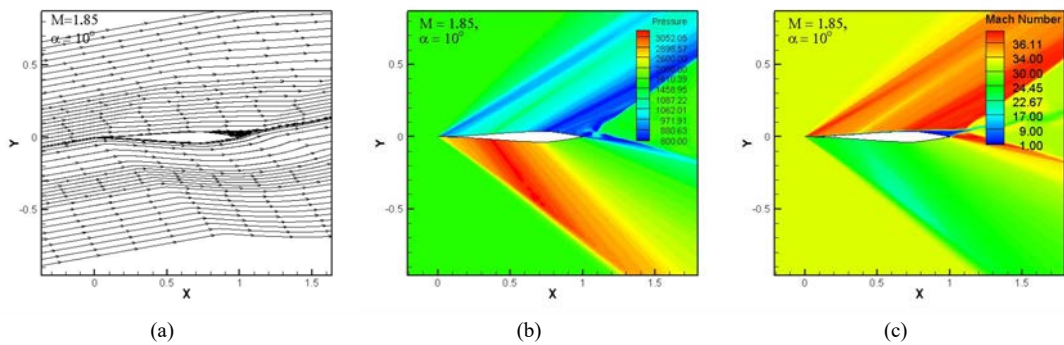
Figure 36 Flow features at $\alpha = 10°$ and M = 2.13, (a) streamlines (b) pressure contours (c) Mach contours (see online version for colours)

(a)

(b)

(c)
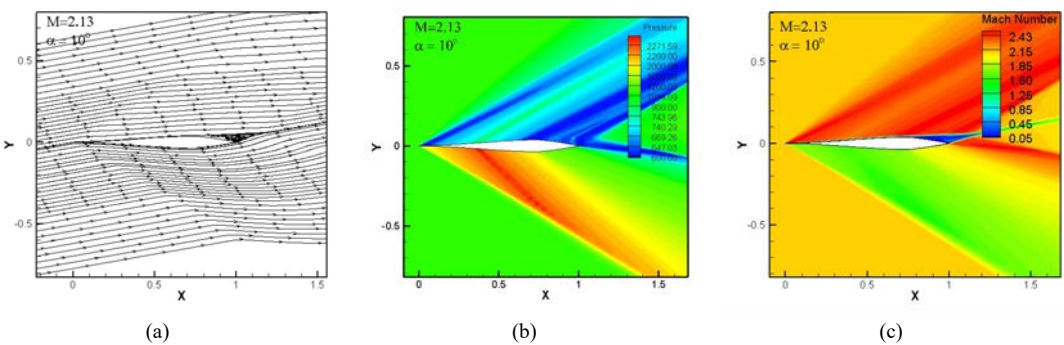
Figure 37 Pressure coefficient (C_P) and skin friction coefficient (C_f) plots at $\alpha = 10°$ and M = 1.25

(a)   (b)
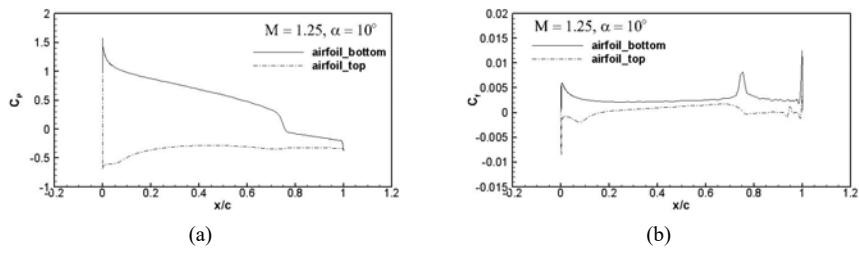
Figure 38 Pressure coefficient (C_P) and skin friction coefficient (C_f) Plot at $\alpha = 10°$ and M = 1.50

(a)   (b)
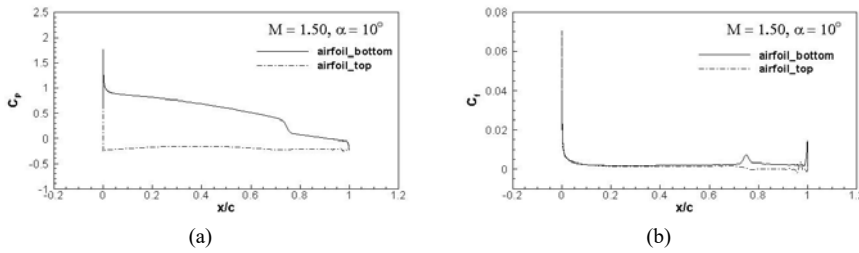
Figure 39 Pressure coefficient (C_P) and skin friction coefficient (C_f) plot at $\alpha = 10°$ and M = 1.85

(a)   (b)
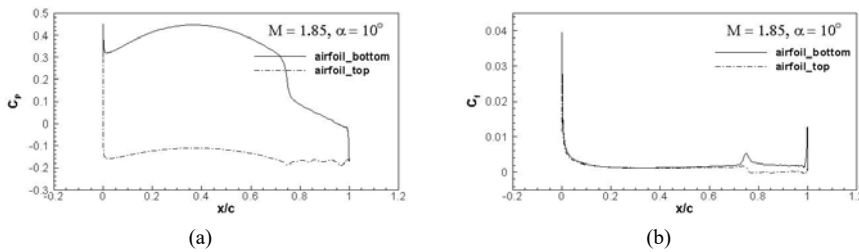
Figure 40 Pressure coefficient (C_P) and skin friction coefficient (C_f) plots at $\alpha = 10°$ and M = 2.13

(a)   (b)
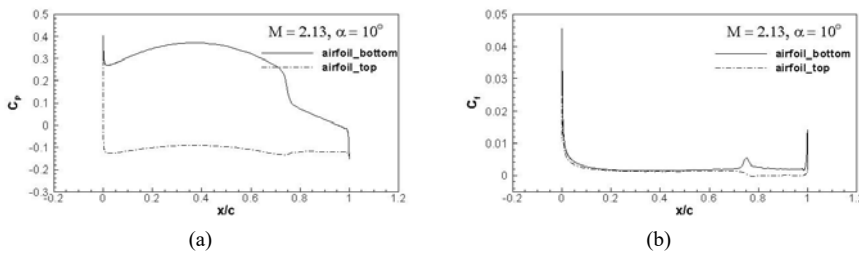
Figure 41 Time histories of drag and lift coefficients at $\alpha = 10°$ and M = 1.25

(a)   (b)
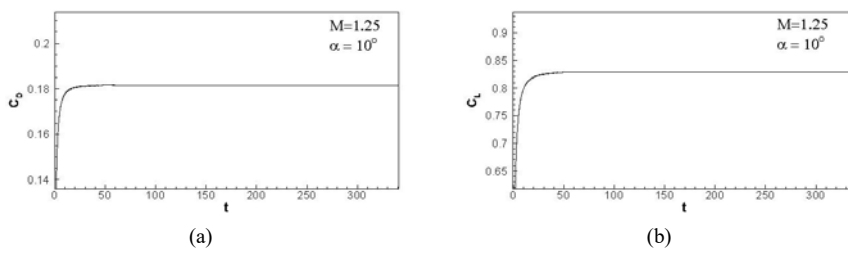
Figure 42 Time histories of drag and lift coefficients at $\alpha = 10°$ and M = 1.50

(a) (b)
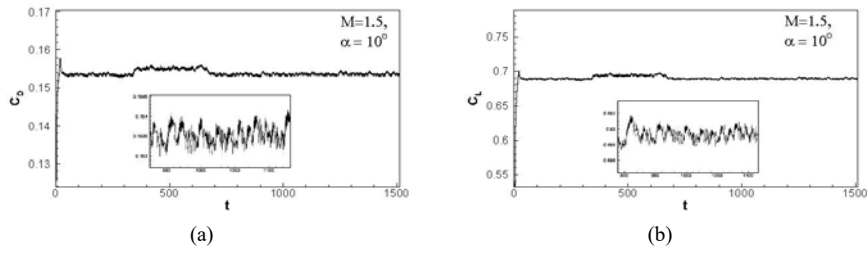
Figure 43 Time histories of drag and lift coefficients at $\alpha = 10°$ and M = 1.85

(a) (b)
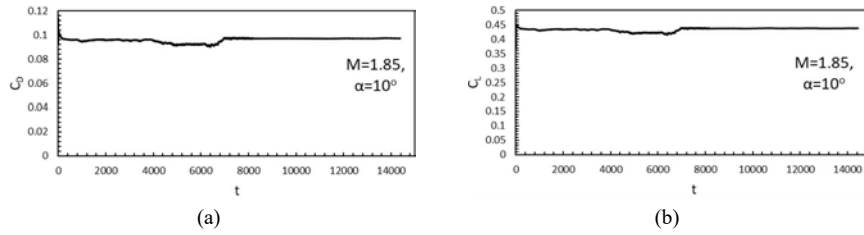
Figure 44 Time histories of drag and lift coefficients at $\alpha = 10°$ and M = 2.13

(a) (b)
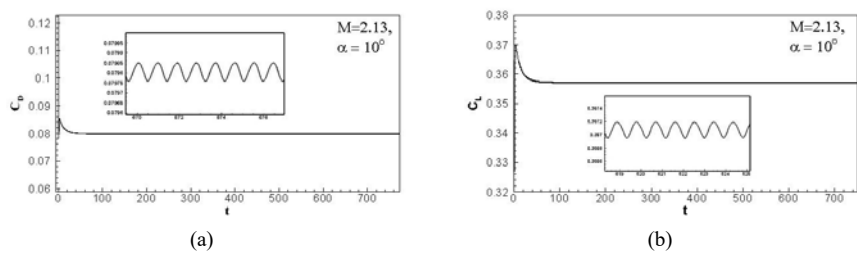
Figure 45 Power spectral distribution of the time histories of C_D and C_L for $\alpha = 10°$ at (a) (b) M = 1.50 (c) (d) M = 1.85

(a) (b)

(c) (d)
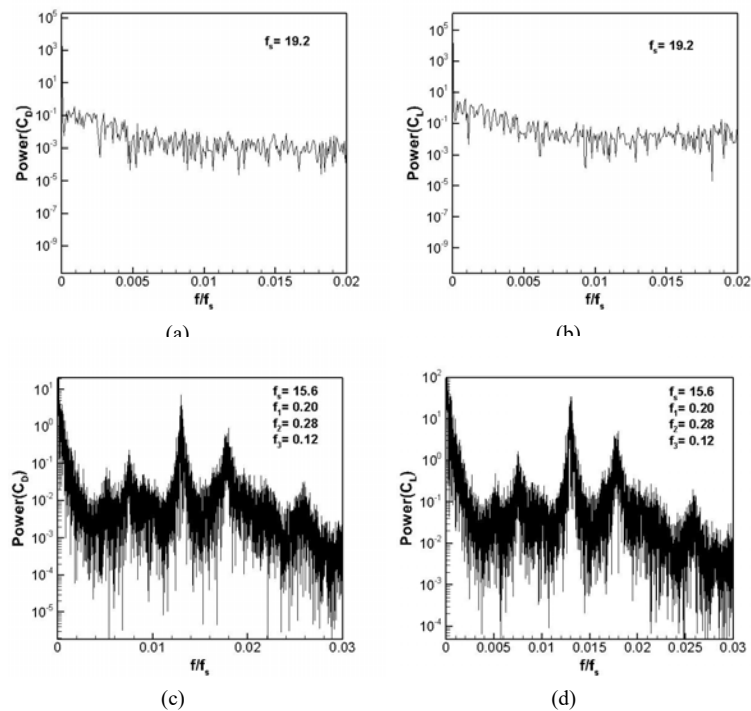
Figure 46   Flow features at $\alpha = 20°$ and M = 1.25, (a) streamlines (b) pressure contours (c) Mach contours (see online version for colours)

(a)   (b)   (c)
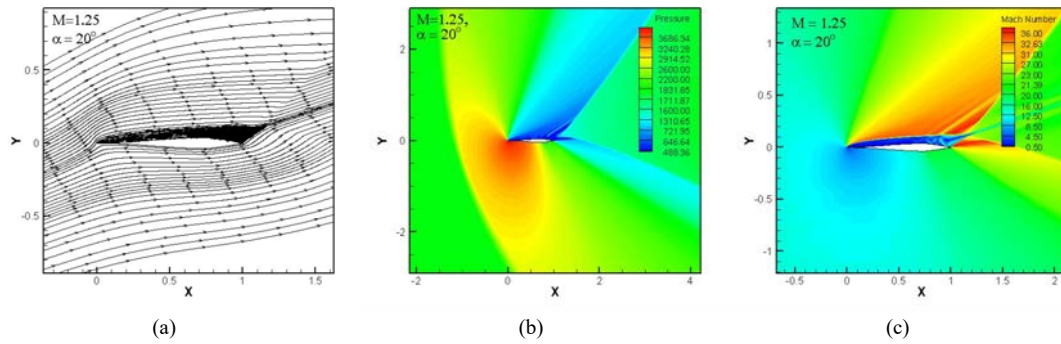
Figure 47   Variation of tangential velocity, temperature and density across the slip lines at $\alpha = 20°$ and M = 1.25

(a)   (b)   (c)
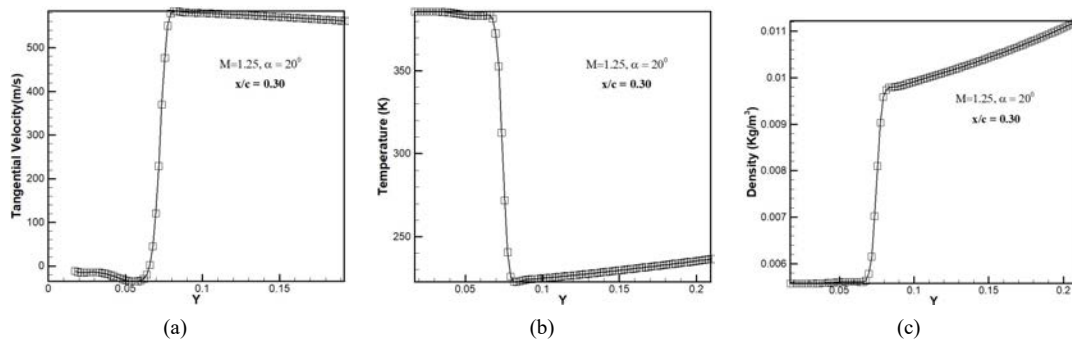
Figure 48   Flow features at $\alpha = 20°$ and M = 1.50, (a) streamlines (b) pressure contours (c) Mach contours (see online version for colours)

(a)   (b)   (c)
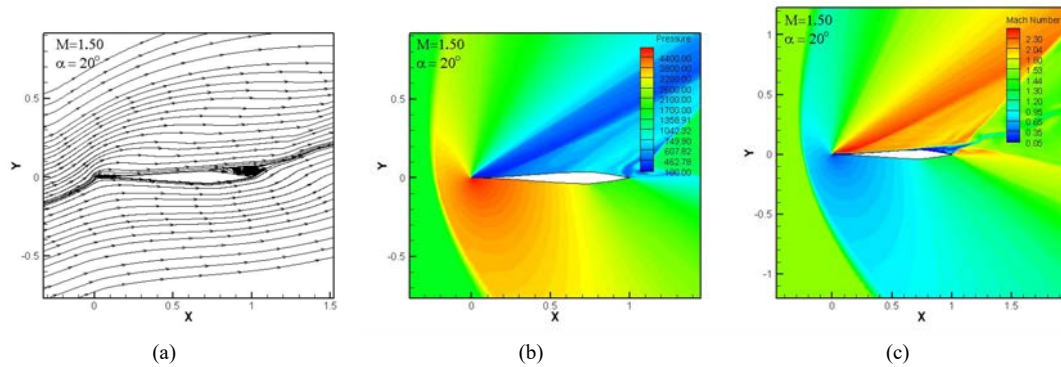
Figure 49   Flow features at $\alpha = 20°$ and M = 1.85, (a) streamlines (b) pressure contours (c) Mach contours (see online version for colours)

(a)   (b)   (c)
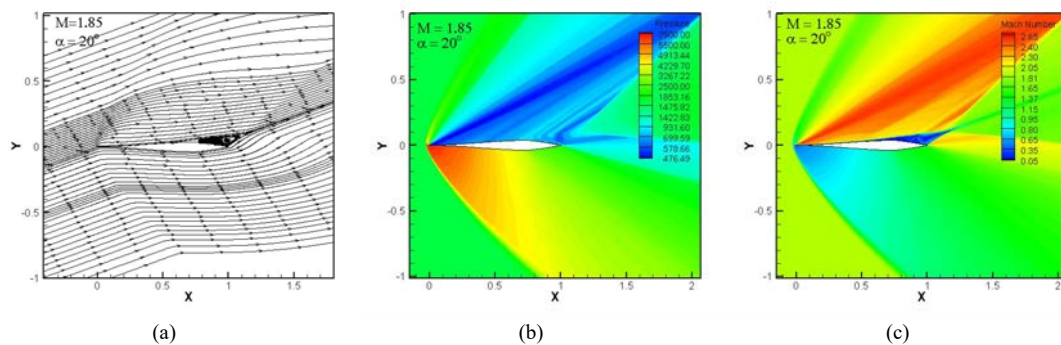
Figure 50 Flow features at $\alpha = 20°$ and M = 2.13, (a) streamlines (b) pressure contours (c) Mach contours (see online version for colours)

(a) (b) (c)
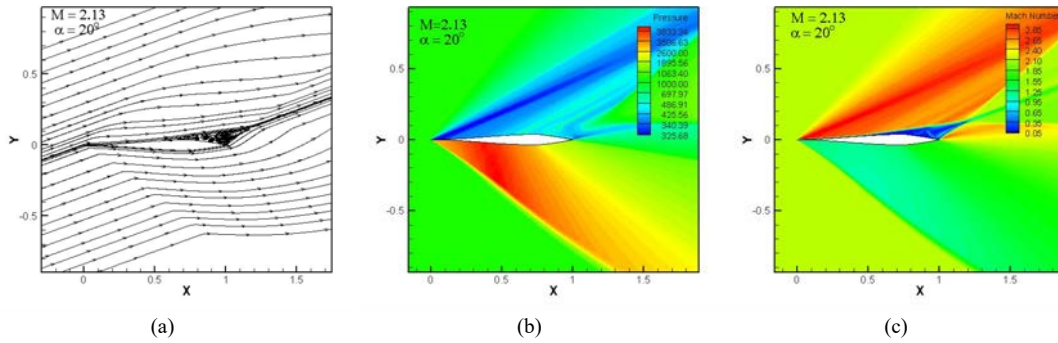
Figure 51 A zoomed view of the flow at the leading edge of the new cusped leading edge airfoil at (a) M = 1.50 and $\alpha = 20°$ (b) M = 1.85 and $\alpha = 20°$

(a) (b)
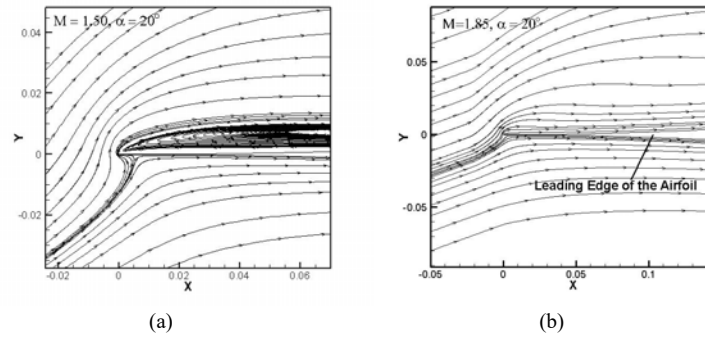
Figure 52 Variation of tangential velocity, temperature and density across the slip lines at $\alpha = 20°$ and M = 1.50

(a) (b) (c)
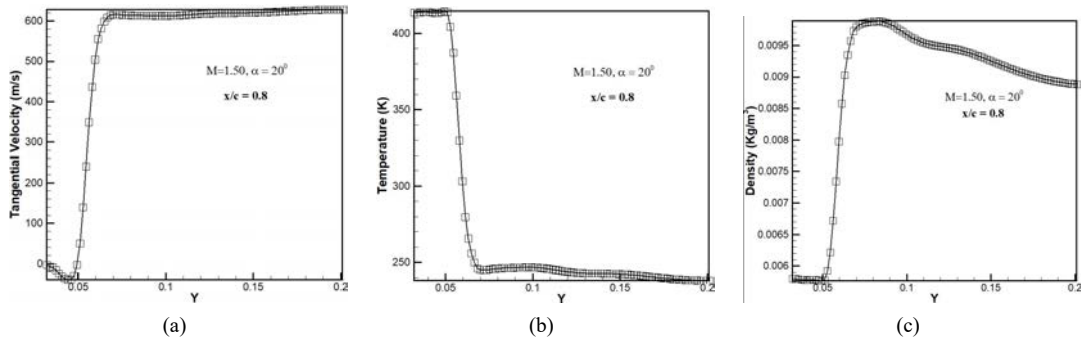
Figure 53 Variation of tangential velocity, temperature and density across the slip lines at $\alpha = 20°$ and M = 1.85

(a) (b) (c)
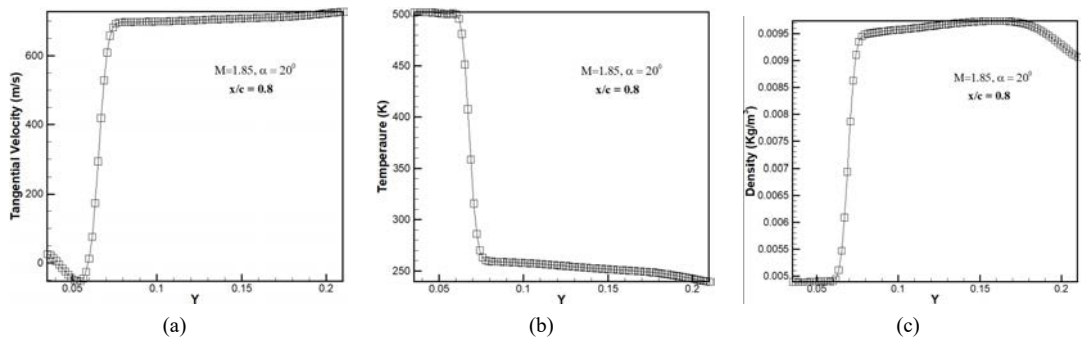
Figure 54   Variation of tangential velocity, temperature and density across the slip lines at $\alpha = 20°$ and M = 2.13

(a)   (b)   (c)
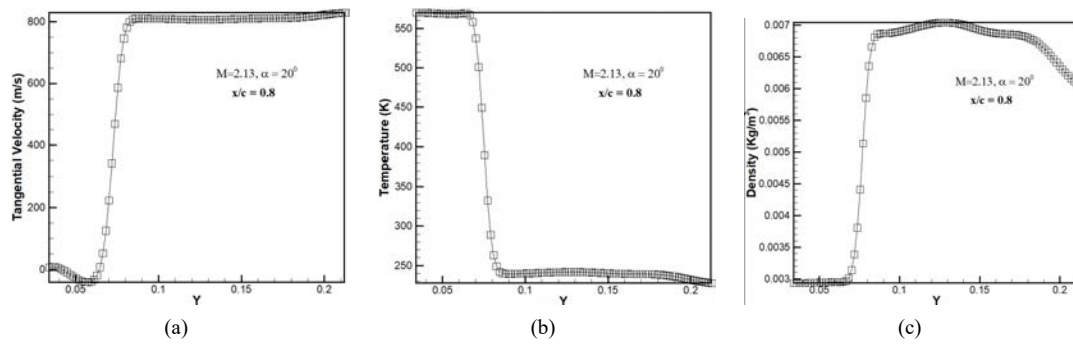
Figure 55   Pressure coefficient (C_P) and skin friction coefficient (C_f) plots at $\alpha = 20°$ and M = 1.25

(a)   (b)
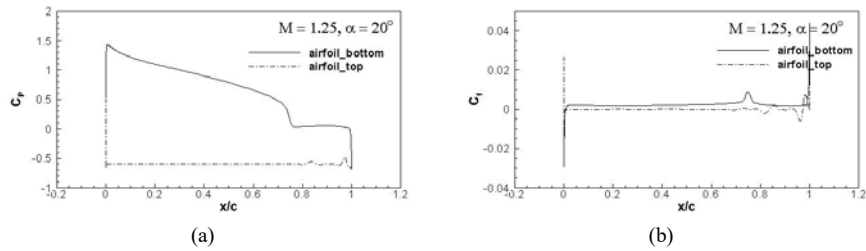
Figure 56   Pressure coefficient (C_P) and skin friction coefficient (C_f) plot at $\alpha = 20°$ and M = 1.50

(a)   (b)
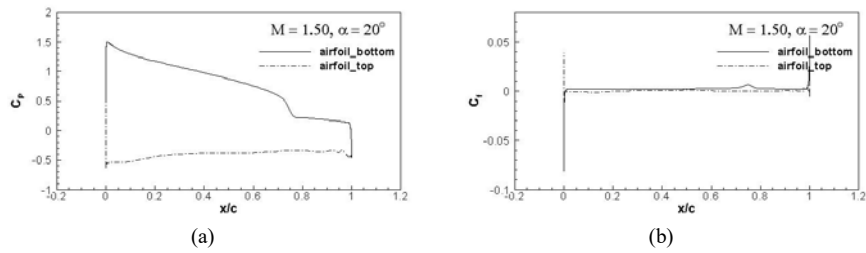
Figure 57   Pressure coefficient (C_P) and skin friction coefficient (C_f) Plot at $\alpha = 20°$ and M = 1.85

(a)   (b)
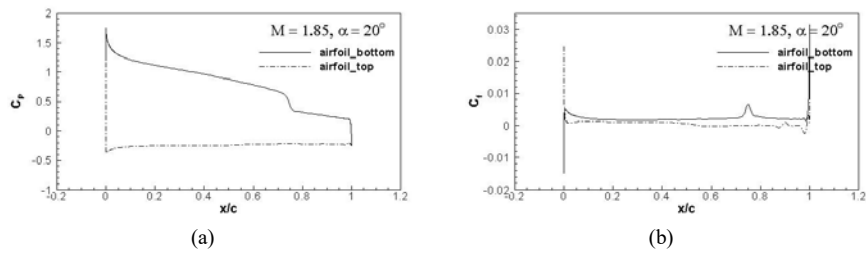
Figure 58   Pressure coefficient (C_P) and skin friction coefficient (C_f) plots at $\alpha = 20°$ and M = 2.13

(a)   (b)
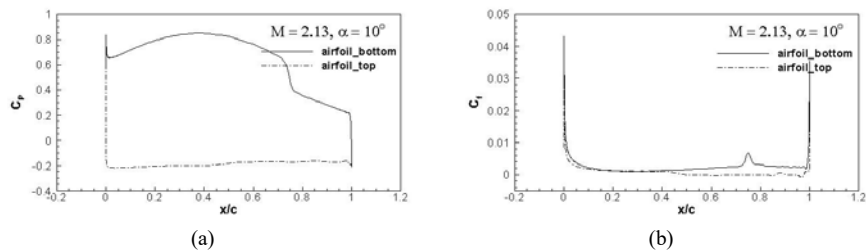
Figure 59 Time histories of drag and lift coefficients at $\alpha = 10°$ and M = 1.25

(a) (b)
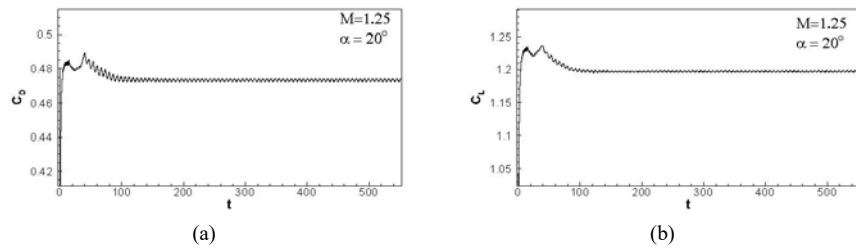
Figure 60 Time histories of drag and lift coefficients at $\alpha = 10°$ and M = 1.50

(a) (b)
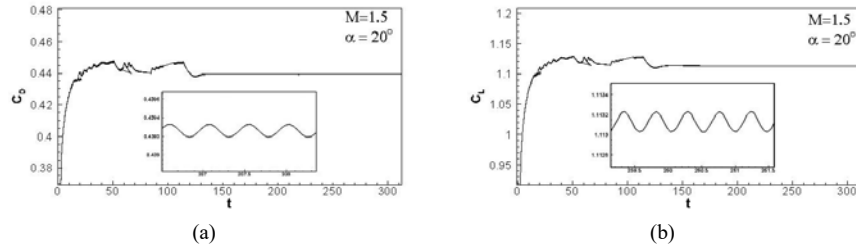
Figure 61 Time histories of drag and lift coefficients at $\alpha = 10°$ and M = 1.85

(a) (b)
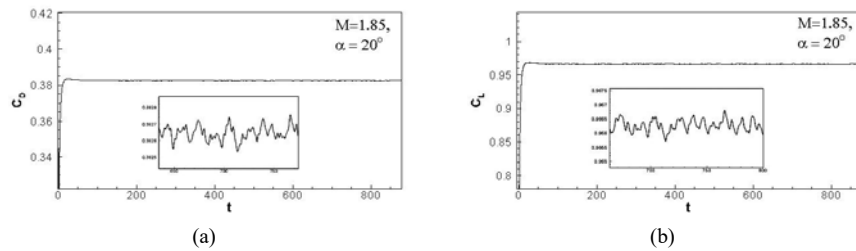
Figure 62 Time histories of drag and lift coefficients at $\alpha = 10°$ and M = 2.13

(a) (b)
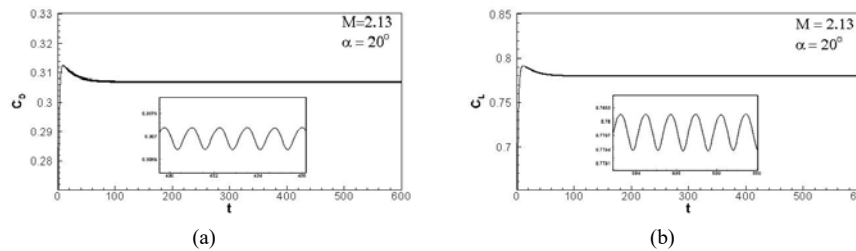
Figure 63 Power spectral distribution of the time histories of C_D and C_L at M = 1.85 and $\alpha = 20°$

(a) (b)
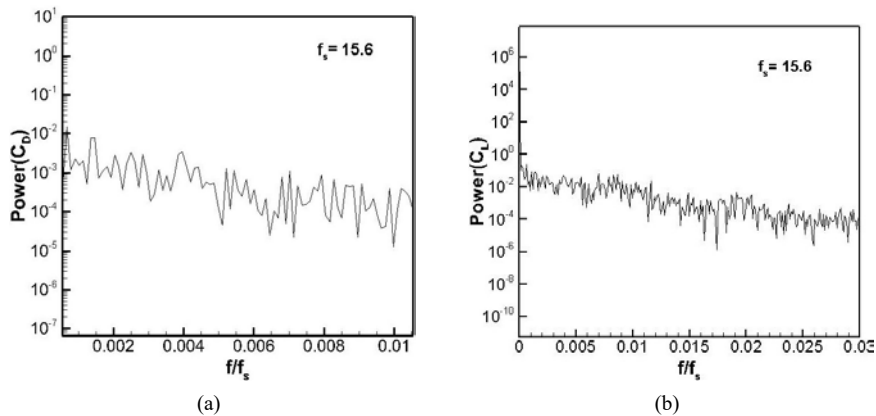
The flow separation at the upper surface is depicted by the C_f plot in Figure 55 as the value of C_f is negative all along the upper surface at M = 1.25. The C_f plot at M = 1.50 shows negative values in the vicinity of leading edge at the upper surface which is a sign of localised flow separation. A highly negative value of C_f at the lower surface near the leading edge is due to the phenomenon of reversed flow at the lower surface of the airfoil. As the flow is inclined at a large angle, the attached flow at the lower surface takes a sharp turn at the trailing edge and hence, the value of C_f is quite large at that point for all the cases.

Figures 59 to 62 show the time histories of global flow parameters at $\alpha = 20°$. The time histories exhibit a decreasing trend of drag and lift with an increase in Mach number. This is due to the movement of the shock wave closer to the airfoil as the Mach number increases. Moreover, the time histories show that the flow is completely periodic in nature for most of the cases at $\alpha = 20°$. The time histories of C_D and C_L have non-dimensional frequencies of 0.17 and 0.14 respectively at M = 1.25 whereas 2.0 for both C_D and C_L at M = 1.50. At M = 1.85, the power spectral distribution (Figure 63) shows a broadband spectrum with dominant dimensionless frequencies in the range of 0.03 to 0.16 for C_D and 0.03 to 0.47 for C_L respectively. At M = 2.13, the flow again becomes periodic with a frequency of 0.8 for both C_D and C_L. A close look at the time histories shows that the unsteadiness is of the order of 10^{-3} to 10^{-4} for all the cases which is quite low.

Figure 64   Identification of steady, periodic and multifrequency flow past the new cusped leading edge airfoil in supersonic regime
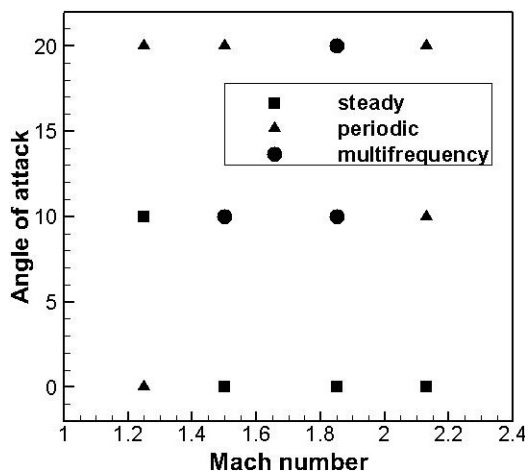
Figure 64 identifies and summarises the various regimes of flow with respect to the Mach number and angle of attack. As is evident from the figure, initially the flow is periodic in nature at $\alpha = 0°$, but becomes completely steady as the Mach number is increased. At $\alpha = 10°$, the flow is steady at Mach 1.25, then transforms into a multifrequency flow at Mach 1.50 and 1.85 and finally becomes periodic at Mach 2.13. Further, the flow is periodic at almost all the Mach numbers at $\alpha = 20°$ except at Mach 1.85 at which it exhibits a multifrequency broadband spectrum. Therefore, it

is apparent that the supersonic flow past the cusped airfoil does not follow any general trend either with Mach number or angle of attack. The transformation of flow dynamics is quite random in nature.

5   Conclusions

It is concluded from the above numerical investigation that the proposed new cusped leading edge airfoil has a much superior aerodynamic characteristics as compared to the conventional biconvex airfoil. The comparison of aerodynamic parameters shows that an almost 40–50% drag reduction is achieved in supersonic regime at $\alpha = 0°$ which is the cruise condition. At higher angles of attack, drag reduction of the order of 17% at $\alpha = 10°$ and 1.2% at $\alpha = 20°$ is achieved at high supersonic Mach numbers when attached oblique shocks start forming. Lift enhancement is observed at low supersonic Mach numbers when stronger detached bow shocks are formed on the new airfoil at all α. The L/D ratio of the new airfoil is higher than the biconvex circular-arc airfoil for almost all the flight conditions. The range of L/D for the new airfoil at $\alpha = 10°$ is 4.5 to 5.5 whereas at $\alpha = 20°$, it is around 2.5. The moment coefficient data shows that the new airfoil has better longitudinal static stability to pitching motion during take-off in supersonic regime as compared to the biconvex airfoil. The supersonic flow past the new airfoil is steady in most of the cases at $\alpha = 0°$. At higher angles of attack, the flow becomes unsteady with periodic nature in some cases while in other cases it exhibits a large number of frequency or time scales in the flow. Furthermore, at $\alpha = 0°$, the rms values are zero while higher fluctuation levels are observed in most of the cases at $\alpha = 10°$ and $\alpha = 20°$. These oscillations may be associated with the trapped vortices in the separated flow regions namely near the leading and trailing edges of the cusped airfoil. Hence, the new cusped airfoil investigated in the present study exhibits improved aerodynamic performance than the conventional airfoil. However, this is only a preliminary work and both conditions of high heat flux, and high stress levels are expected near the leading edge. Therefore, more detailed investigations in various flow regimes are required in order to realise the full potential of the new airfoil geometry for supersonic flight.

References

Akram, S., Hasan, N. and Khan, A. (2013) 'Numerical investigation of viscous laminar supersonic flow past an asymmetric biconvex circular-arc aerofoil', *Applied Mechanics and Materials*, Vol. 390, No. 3, pp.147–151.

Alexander, K. (2008) 'Bifurcations of transonic flow past flattened airfoils', *Keynote Lecture at the Fifth International Conference on Computational Fluid Dynamics*, Seoul National University, Korea, No. 1, pp.1–11.

ANSYS, Inc. (2013) *Ansys® Fluent Theory Guide, Release 15.0, Help System, Basic Fluid Flow*, pp.1–16.

Ashill, P.R., Fulker, J.L., Simmons, M.J. and Gaudet, I.M. (1996) 'A review of research at dra on active and passive control of shock waves', *ICAS Congress, 20th, Proc.*, Naples, Italy, Vol. 1, pp.76–87, AIAA, Reston, VA.

Ayers, T.G. and Hallissy, J.B. (1981) *Historical Background and Design Evolution of the Transonic Aircraft Technology and Supercritical Wing*, NASA TM 81356, Dryden Flight Res. Center, Edwards, CA.

Bahi, L., Ross, J.M. and Nagamatsu, H.T. (1983) 'Passive shockwave/boundary layer control for transonic airfoil drag reduction', Presented at *AIAA Aerosp. Sci. Meet., 21st*, Reno, NV.

Banas, K. (2020) 'The requirements for the turbulence models in application to heat transfer analysis of turbine parts: the thermal stresses point-of-view', *Progress in Computational Fluid Dynamics, an International Journal*, Vol. 20, No. 4, pp.187–200.

Bur, R., Corbel, B. and Jean, D. (1998) 'Study of passive control in a transonic shock wave/boundary-layer interaction', *AIAA Journal*, Vol. 36, No. 3, pp.394–400.

Bushnell, D.M. (2004) 'Shock wave drag reduction', *Annual Review of Fluid Mechanics*, Vol. 36, No. 1, pp.81–96.

Bushnell, D.M. and Huffman, J.K. (1968) *Forward Penetration of Liquid Water and Liquid Nitrogen Injected from an Orifice at the Stagnation Point of a Hemispherically Blunted Body in Hypersonic Flow*, NASA TM X-1493, Langley Res. Cent., Hampton, VA.

Chapman, D.R. (1955) *Reduction of Profile Drag at Supersonic Velocities by the Use of Airfoil Sections Having a Blunt Trailing Edge*, NACA TN 3505, Ames Aeronaut. Lab., Moffett Field, CA.

Charczenko, N. and Hennessey, K.W. (1961) *Investigation of a Retrorocket Exhausting from the Nose of a Blunt Body into a Supersonic Free Stream*, NASA TN, D-751.

Chen, C-L., Chow, C-Y., Holst, T.L. and van Delsem, W.R. (1985) 'Numerical simulation of transonic flow over porous airfoils', Presented at *3rd AIAA Appl. Aerodyn. Conf.*, Colorado Springs, CO.

Deshpande, V., Eshpuniyani, B. and Sanghi, S. (2015) 'Computational study of supersonic flow past non-stationary obstructions part-i – moving ramp', *Progress in Computational Fluid Dynamics, an International Journal*, Vol. 15, No. 3, pp.144–156.

Garanin, A. (2000) 'Pressure variation on the face of the body of revolution with a spike with variation of its length, geometry and injection of an inert gas from the spike', *International Conferences on Methods of Aerophysical Research, Proc.*, Part 1(A00-41738 11-34), Russ. Acad. Sci., Novosibirsk Tomsk, Russia, pp.94–97.

Geoggievskii, P.Y. and Lenin, V.A. (1988) 'Supersonic flow around objects with external heat evolution sources', *Soviet Technical Physics Letter*, Vol. 14, No. 4, pp.303–304.

Gilinsky, M., Blankson, I., Sakharov, V.I. and Shvets, A.I. (2001) 'Shock waves mitigation at blunt bodies using needles and shells against a supersonic flow', Presented at *AIAA/ASME/SAE/AEE Jt. Propuls. Conf., 37th*, Salt Lake City, UT.

Gillan, M.A. (1993) 'Computational analysis of drag reduction and buffet alleviation in viscous transonic flow over porous airfoils', *11th Applied Aerodynamics Conference*, American Institute of Aeronautics and Astronautics.

Golovitchev, V.I. and Hansson, J. (1998) 'Some trends in improving hypersonic vehicles aerodynamics and propulsion', Presented at *AIAA Int. Symp. Air-breathing Eng., 14th*, Florence, Italy.

Gupta, A. and Ruffin, S.M. (1999) 'Optimal artificially blunted leading-edge airfoils for enhanced aerothermodynamic performance', *Journal of Spacecraft and Rockets*, Vol. 36, No. 4, pp.499–506.

Gupta, A., Ruffin, S.M., Newfield, M.E. and Yates, L. (2000) 'Aerothermodynamic performance enhancement of sphere-cones using the artificially blunted leading-edge concept', *Journal of Spacecraft and Rockets*, Vol. 37, No. 2, pp.235–241.

Guy, Y., McLaughlin, T. and Morrow, J. (2001) 'Blunt body wave drag reduction by means of a standoff spike', *39th Aerospace Sciences Meetings*, American Institute of Aeronautics and Astronautics.

Hsieh, S-J. and Lee, L-C. (1989) 'Numerical simulation of transonic porous airfoil flows', *International Symposium on Numerical Methods in Engineering*, Computational Mechanics, Boston, Vol. 1, pp.601–608.

Ibrahim, I., Ng, E. and Wong, L. (2010) 'Effect of the angle of attack on the YF-16 inlet', *International Journal of Aerodynamics*, Vol. 1, No. 2, pp.169–191.

Jones, E.P., Townsend, S.M., Guy, Y. and McLaughlin, T.E. (2000) 'Reduction of the wave drag of a blunt body by means of a standoff spike', Presented at *AIAA Aerosp. Sci. Meet., 38th*, Reno, NV.

Karlovskii, V.N. and Sakharov, V.I. (1986) 'Numerical investigation of supersonic flow past blunt bodies with protruding spikes', *Fluid Dynamics*, Vol. 21, No. 3, pp.437–445.

Kijima, M., Kubota, H., Watanuki, T. and Fujita, M. (1996) 'Effect of nose configuration of spike on reduction of pressure drag in hypersonic flow', *Strengthening Cooperation in the 21st Century: Proc. 6th Int. Space Conf.*, Pac. Basin Soc., pp.273–284.

Kuzmin, A. (2015) 'Lift sensitivity analysis for a Whitcomb airfoil with aileron deflections', *Progress in Computational Fluid Dynamics, an International Journal*, Vol. 15, No. 1, pp.10–15.

Love, E.S. (1952) *The Effects of a Small Jet of Air Exhausting from the Nose of a Body of Revolution in Supersonic Flow*, NACA RM L52I19a.

Magi, E.C. and Gai, S.L. (1998) 'Flow behind castellated blunt-trailing-edge aerofoils at supersonic speeds', *Journal of Fluid Mechanics*, Vol. 375, No. 1, pp.85–111.

Mayer, J.P. (1949) *Estimation of Lift and Drag of Airfoils at Near Sonic Speeds and in the Presence of Detached Shock Waves*, NACA RM No. L8L07.

Meyer, B., Nelson, H.F. and Riggins, D.W. (2001) 'Hypersonic drag and heat-transfer reduction using a forward-facing jet', *Journal of Aircraft*, Vol. 38, No. 4, pp.680–686.

Myrabo, L.N. and Raizer, Y.P. (1994) 'Laser induced air spike for advanced transatmospheric vehicles', Presented at *Plasmadyn. Lasers Conf., 25th*, Colorado Springs, CO.

Raghunathan, S. (1987) 'Effect of porosity strength on passive shock-wave/boundary-layer control', *AIAA Journal*, Vol. 25, No. 5, pp.757–758.

Raghunathan, S., Gray, J. and Cooper, R. (1987) 'Effect of inclination of holes on passive shock wave boundary layer control', *25th Aerospace Sciences Meetings*, American Institute of Aeronautics and Astronautics.

Raj, P. and Miranda, L.R. (1981) 'A cost effective method for shockfree supercritical wing design', Presented at *AIAA Aerosp. Sci. Meet., 19th*, St. Louis, MO.

Redeker, G., Wichmann, G. and Oelker, H.C. (1986) 'Aerodynamic investigations toward an adaptive airfoil for a transonic transport aircraft', *Journal of Aircraft*, Vol. 23, No. 5, pp.398–405.

Reding, J.P., Guenther, R.A. and Richter, B.J. (1977) 'Unsteady aerodynamic considerations in the design of a drag-reduction spike', *Journal of Spacecraft and Rockets*, Vol. 14, No. 1, pp.54–60.

Reding, J.P. and Jecmen, D.M. (1983) 'Effects of external burning on spike-induced separated flow', *Journal of Spacecraft and Rockets*, Vol. 20, No. 5, pp.452–453.

Reneaux, J. and Coustols, E. (1999) 'Wave drag reduction technologies', Presented at *ONERADLR Aerosp. Symp.*, Paris.

Riggins, D.W. and Nelson, H.F. (2000) 'Hypersonic flow control using upstream focused energy deposition', *AIAA Journal*, Vol. 38, No. 4, pp.723–725.

Riggins, D.W., Nelson, H.F. and Johnson, E. (1999) 'Blunt-body wave drag reduction using focused energy deposition', *AIAA Journal*, Vol. 37, No. 4, pp.460–467.

Romeo, D.J. and Sterrett, J.R. (1963) *Exploratory Investigation of the Effect of a Forward Facing Jet on the Bow Shock of a Blunt Body in a Mach Number 6 Free Stream*, NASA TN D-1605.

Rosemann, H., Birkemeyer, J. and Knauer, A. (2000) 'Shock control by adaptive elements for transportation aircraft wings', *Active Control Technology for Enhanced Performance Operational Capabilities of Military Aircraft, Land Vehicles, and Sea Vehicles*, Inst. Ström, Germany, pp.16.1–16.6.

Ruffin, S.M., Gupta, A. and Marshall, D. (2000) 'Supersonic channel airfoils for reduced drag', *AIAA Journal*, Vol. 38, No. 3, pp.480–486.

Schmitt, V. and Destarac, D. (1998) 'Recent progress in drag prediction and reduction for civil transport aircraft at Onera', *Aerospace Sciences Meetings*, American Institute of Aeronautics and Astronautics.

Selvaraj, R.M., Paul, P.E.S., Kumar, G.U. and Ramesh, M. (2017) 'Optimisation of swept angles for airfoil NACA 6-series', *International Journal of Computer Aided Engineering and Technology*, Vol. 9, No. 2, pp.229–240.

Walters, D.K. and Blades, E.L. (2011) 'Critical assessment of hybrid and zonal wall functions for missile aerodynamics simulations', *Progress in Computational Fluid Dynamics, an International Journal*, Vol. 11, No. 6, pp.335–349.

Whitcomb, R.T. (1974) 'Review of nasa supercritical airfoils', Presented at *Congr. Int. Counc. Aeronaut. Sci., 9th*, Haifa, Israel.

Yamauchi, M., Fujii, K., Tamura, Y. and Higashino, F. (1993) 'Numerical investigation of supersonic flows around a spiked bluntbody', Presented at *AIAA Aerosp. Sci. Meet. Exhib., 31st*, Reno, NV.

Nomenclatures

C_D	Drag coefficient.
C_L	Lift coefficient.
C_P	Pressure coefficient.
C_M	Moment coefficient.
L/D	Lift to drag ratio.
$C_{D,biconvex}$	Drag coefficient of conventional biconvex circular arc airfoil.
$C_{L,biconvex}$	Lift coefficient of conventional biconvex circular arc airfoil.
$C_{M,biconvex}$	Moment coefficient of conventional biconvex circular arc airfoil.
$C_{D,cusped}$	Drag coefficient of the new cusped leading edge airfoil.
$C_{L,cusped}$	Lift coefficient of the new cusped leading edge airfoil.
$C_{M,cusped}$	Moment coefficient of the new cusped leading edge airfoil.
$(L/D)_{biconvex}$	Lift to drag ratio of conventional biconvex circular arc airfoil.
$(L/D)_{cusped}$	Lift to drag ratio of the new cusped leading edge airfoil.
ΔC_D	$C_{D,cusped} - C_{D,biconvex}$.
ΔC_L	$C_{L,cusped} - C_{L,biconvex}$.
$\Delta(L/D)$	$(L/D)_{cusped} - (L/D)_{biconvex}$.
C_f	x-component of xkin friction coefficient.
c	Chord length of the airfoil.
x_m	Location of maximum thickness of the airfoil along the chord.
y_m	Maximum thickness of the airfoil from the chord.
l	Characteristic length (chord length of the airfoil).
M	Free stream Mach number.
Re	Free stream Reynolds number.
δ	Leading edge angle or deflection angle.
α	Angle of attack.
t	Dimensionless time.
$\bar{t}$	Time in seconds.
U_∞	Free stream velocity in m/s.